

Scale factor determination of spring type gravimeters in the amplitude range of tides by a moving mass device

A Koppán¹, J Benedek², M Kis¹, B Meurers³ and G Papp² 

¹ Mining and Geological Survey of Hungary, 1145 Budapest, Hungary

² Geodetic and Geophysical Institute, Research Centre for Astronomy and Earth Sciences, Hungarian Academy of Sciences, 9400 Sopron, Hungary

³ Department of Meteorology and Geophysics, University of Vienna, 1090 Wien, Austria

E-mail: papp.gabor@csfk.mta.hu

Received 4 February 2019, revised 15 August 2019

Accepted for publication 27 August 2019

Published 23 January 2020



Abstract

This paper investigates the characteristics and the metrological limits of the calibration of spring type gravimeters by using a cylindrical test mass moved vertically around the gravimeter by a lifting device operated in the Mátyáshegy Observatory. The movement of the 3100 kg iron mass generates a sinusoid-like calibrating signal having a peak-to-peak amplitude of 1102 nm s^{-2} . The careful determination of the geometrical and physical parameters of the test mass combined with the analytical modeling of its gravitational effect and the related uncertainties provides an accuracy of 3 nm s^{-2} in absolute sense. The overall accuracy, however, is influenced by several other instrumental and environmental factors which are investigated in detail. The conclusions are based on more than 400 experiments with 5 LCR G instruments. As a unique case a Scintrex CG-5 instrument was also involved in the tests what is probably the very first moving mass calibration of this type of gravimeters.

Two processing methods, *Max-Min* and *Full-Fit*, based on L2 norm adjustment of the observations were developed and applied to obtain instrumental scale factor and other related parameters.

The results show that the observations corrected for the disturbing effects still contain a systematic constituent with amplitude of $(10\text{--}20) \text{ nm s}^{-2}$ regardless which LCR instrument was calibrated. It resembles the second time derivative of the calibrating signal that may indicate the non-uniform elastic response of the spring sensors to the rate of gravity change. Due to the problems mentioned above the overall dispersion of the resultant random and non-random residuals of the calibration observations provided by *Full-Fit* method are typically 10 nm s^{-2} . The *a posteriori* standard deviations of the individual scale factors provide, however, measurement accuracy of 2 nm s^{-2} .

Keywords: moving mass device, accuracy limits, LCR G gravimeters, Scintrex CG-5 gravimeters, cylindrical ring mass, calibration of gravimeters

 Supplementary material for this article is available [online](#)

(Some figures may appear in colour only in the online journal)

1. Introduction

The most dominant source of the periodic time variation of gravity acceleration g is the tidal phenomenon but other,

sometimes very complex hydrology- and weather related environmental processes causing temporal change of the mass distribution of the Earth have also significant contribution in various segments of the full spectrum of time variation.

Consequently all of those corrections which have to be applied to obtain a representative gravity acceleration value at a point on the earth's surface free of any short term influences must be considered and modeled at the highest available accuracy.

The most advanced instrumentation for tidal investigation is based on superconducting gravimeters (SG) commonly calibrated by comparison with co-located absolute gravimeters (AG). Both instruments are expensive and hence not available everywhere. However, a low cost technology might be sufficient for deriving tidal models fulfilling the accuracy requirements of even precise field gravimetry. It is based on co-located relative gravimeters like LaCoste-Romberg (LCR) (e.g. Pálinkáš 2006) and/or Scintrex CG-5 gravimeters (Meurers 2012, Benedek *et al* 2014, Papp *et al* 2018).

In order to make this obsolete instrumentation applicable for e.g. long-term tidal recording or microgravimetric (laboratory) measurements, one needs careful examination of the LCR sensor characteristics (Götze and Meurers 1983) and adequate correction of distorting instrumental effects. For instance, sensitivity on tilt, temporal change of scale factors and beam-position dependent scale functions must be determined for observatory use of these instruments.

The scale factor s of the instruments, defined as the ratio of reference and observed gravity changes, may vary in time regardless if the gravimeters are equipped with feed-back systems or not. Furthermore, in the latter situation, the scale factor depends also on the index-beam position x_{ib} . Then, a function S has to be determined within the full measuring range of the sensor instead of a single scale factor value:

$$s = S(x_{ib}). \quad (1)$$

There are different ways to determine the scale factor or scale factor function of a gravimeter. The relative method is based on comparing the observations \hat{g} given in any unit (e.g. mV, pixel, ...) to measurements of a reference instrument \hat{g}_{ref} or gravity data Γ (given in nm/s^2) provided by a specific tidal model after removing any systematic instrumental and environmental signals (drift, air pressure variation, etc...), which are not common in both time series:

$$S(x_{ib}) = \hat{g}_{ref}/\hat{g}, \quad (2)$$

$$S(x_{ib}) = \Gamma/\hat{g}. \quad (3)$$

In equations (2) and (3), the model errors of the non-common systematic signals and random noise influence the determination of $S(x_{ib})$. In equation (3), Γ is just an estimate of the true tides at specific location and time, regardless it is derived from a theoretical model or from observations, and hence not a real standard in the sense of metrology.

The relative method is commonly applied by collocated observations with AGs (Hinderer *et al* 1991, Francis *et al* 1998), periodic platform movement (Richter *et al* 1995) or well-calibrated spring gravimeters (Meurers 2012, Riccardi *et al* 2012). However, even if AGs providing the absolute value g of the gravity vector are involved, the obtained scale factors cannot be called absolute in the rigorous sense of metrology as not pure standards but individual instruments composed of very complex physical systems are compared through their

observations. A moving test mass is an undoubtedly simpler 'instrument' and a more robust (time invariant) standard than an AG the time variant accuracy and performance of which depends on very sophisticated and sensitive electrical, mechanical and optical components. Obviously the gravitational effect of a test mass as a derived metrological standard has also uncertainties. However, as will be demonstrated, it is well below the microgal level and depends on only a few other basic standards like mass, length and the gravitational constant G . Moreover, using AGs or relative gravimeters as reference requires the validity of the assumption that all sensors experience the same gravity signal. However, this is never fulfilled exactly due to the spatial and temporal separation of the sensors so the theoretical requirement of constrained centricity and synchrony derived as an analogy of Abbe principle of alignment is violated. These constraints, however, can be provided by the moving mass device due to the geometry of cylindrical ring mass much more rigorously.

The absolute method is based on comparing observations to a physically realized reference (Newtonian) signal \tilde{g} generated by e.g. moving a test mass in a metrologically well-controlled way:

$$S(x_{ib}) = \tilde{g}/\hat{g}. \quad (4)$$

Warburton *et al* (1975) have firstly applied this absolute method, called moving mass calibration (MMC) in the following, for the calibration of SGs. They used a 321 kg hollow steel sphere filled with mercury to generate a $\sim 100 \text{ nm s}^{-2}$ test signal. Achilli *et al* (1995) obtained a 67 nm s^{-2} effect by lifting a ring mass of 272 kg around the T015 SG reaching a precision of 0.3% for the derived calibration factor.

The idea of MMC using a heavy cylindrical ring (about 3100 kg) was described by Barta *et al* (1986). The device developed for LCR gravimeters was installed in the Mátyáshegy Gravity and Geodynamic Observatory in 1990 (Varga *et al* 1995). The aim was to provide a relative accuracy of 0.1%–0.2% for the calibration of spring-type gravimeters recording Earth tides. Although the device was used many times in the past, the huge magnetic effect of the steel cylinder on the metal spring of the LCR sensors was not recognized and handled. Thanks to the financial support of the Hungarian National Research Found Project Number K101603 the methodology of MMC could be revisited and partly improved. In this paper the main problems of this method in terms of modeling accuracy, observation precision and environmental effects are investigated in detail.

2. The Mátyáshegy MMC device

Csapó and Szatmári (1995) describe the physical and geometrical properties of the cylinder made of steel. The total mass is $3103.765 \pm 0.021 \text{ kg}$ with a height of 1030 mm, an inner diameter of 320 mm and an outer diameter of 770 mm. The maximum (peak-to-peak) theoretical gravity variation produced by the moving the mass vertically along the vertical symmetry axis is $1102.48 \text{ nm s}^{-2}$ ($G = 6.672 \times 10^{-11} \text{ m}^3 \text{ kg}^{-1} \text{ s}^{-2}$). A massive suspension construction with high load capacity and

a frequency driven winch provide a smooth up and down movement of the mass, which is controlled by a PLC-programmed system. Different measurement schemes with different parameters such as speed of movement, number of up and down cycles, one or more (up to 15) stops (mass positions and waiting times) during a cycle can be preset. The system outputs the vertical position of the mass in units of millimeters. The positioning accuracy is 0.1 mm. However, two consecutive outputs c and d are rounded to integer numbers, therefore the standard deviation of rounding (Joglekar 2003), assuming uniform error distribution, is

$$\frac{(c - d)}{\sqrt{12}} = \frac{1 \text{ mm}}{3.46} = 0.29 \text{ mm.}$$

An ICP-DAS 7017 type A/D converter with 16-bit resolution, or alternatively a special A/D converter with 22-bit resolution is used to digitize analogue outputs (CPI, electric level output, etc) of the tested gravimeters. A Linux based data acquisition system running on an industrial PC collects the digitized data and records all the necessary parameters with 1 Hz sampling rate. The whole system (figure 1) can be controlled remotely through the Internet. If the gravimeter data is recorded by a separate computer, like in case of the electro-optical readout (Papp et al 2018), the independent components of the whole recording system have to be synchronized to a common time server.

3. Methods of scale factor determination

Two different methods are applied:

1. *Max-Min* method: the scale factor s as a function of x_{ib} (see equation (4)) is determined as the quotient of maximal theoretical and measured variations $\Delta\tilde{g} = \tilde{g}_{\max} - \tilde{g}_{\min}$ and $\Delta\hat{g} = \hat{g}_{\max} - \hat{g}_{\min}$ respectively, generated by the moving mass:

$$s = S(x_{ib}) = \Delta\tilde{g}/\Delta\hat{g}. \quad (5)$$

2. *Full-Fit* method: the scale factor is determined by fitting the observed gravity signal to the theoretical one over the full range of the reference signal following the common scheme of least squares adjustment:

$$\hat{g}(l_i) + e_i = k\tilde{g}(h_0 - l_i) + g_0 \quad (6)$$

where l_i is the measured instantaneous height of the top of the moving cylinder, $k = s^{-1}$ is the inverse of the unknown scale factor (equation (4)) given at a certain x_{ib} , h_0 is the unknown vertical distance between the gravimeter sensor and the top of the moving mass in its initial position ($l_i = 0$), g_0 is the unknown gravity value in the initial position of the moving mass ($l_i = 0$) and e_i is the correction of observation provided by the general L2 norm condition:

$$\sum_{i=1}^N p_i e_i^2 \rightarrow \min, \quad (7)$$

where N is the number of observations and p_i is the weight of the i th observation.

Before applying both methods, time dependent corrections $g_{\text{drift}}(t)$, $g_{\text{tide}}(t)$, $g_{\tau}(t)$, $g_p(t)$ for drift, tides, tilt and air pressure respectively make the raw data free from any short-periodic gravity fluctuations not contained in the reference signal. The magnetic effect of the moving steel mass has to be also considered. The detailed discussion on corrections is given in section 5.

According to e.g. Setiawan (2003), the theoretical gravity effect of the cylindrical body reads as:

$$\tilde{g}(h_0 - l_i) = 2\pi G\Delta\rho \left(\sqrt{(h_0 - l_i)^2 + r_1^2} - \sqrt{(h_0 - l_i + L)^2 + r_1^2} - \sqrt{(h_0 - l_i)^2 + r_2^2} + \sqrt{(h_0 - l_i + L)^2 + r_2^2} \right) \quad (8)$$

where l_i and h_0 are defined as in equation (6); r_1 and r_2 are the outer and inner cylinder radius; L denotes the cylinder height and $\Delta\rho$ is the density difference between steel and air (figure 2a).

During the vertical movement of the cylindrical mass the recorded signal $g(l)$ shows a sinusoid-like shape (figure 2b) with definite extremes if the start and end positions of the mass are sufficiently below and above the sensor of the gravity meter, respectively.

In the *Max-Min* method only the maximum and minimum values of the tide- and drift free observations \hat{g}_{\max} and \hat{g}_{\min} are determined. The difference

$$\Delta\hat{g} = \hat{g}_{\max} - \hat{g}_{\min} = \max(\hat{g}) - \min(\hat{g}) = \max(g(t) - g_{\text{drift}}(t) - g_{\text{tide}}(t) - g_{\tau}(t) - g_p(t)) - \min(g(t) - g_{\text{drift}}(t) - g_{\text{tide}}(t) - g_{\tau}(t) - g_p(t)) \quad (9)$$

can be directly compared to the theoretical value $\Delta\tilde{g}$. The scale factor results from applying equation (4) with $\tilde{g} = \Delta\tilde{g}$ and $\hat{g} = \Delta\hat{g}$. Equation (9) provides the gravity meter response $\Delta\hat{g}$ to the gravitational change generated by the mass movement.

The maximum and minimum values of the observations can be simply obtained by fitting n degree polynomials

$$\hat{g}(l) \cong \hat{g}_n(l) = \sum_{k=0}^n a_k l^k, \hat{g}(l) \cong \hat{g}_n(l) = \sum_{k=0}^n b_k l^k \quad (10)$$

locally (e.g. in L2 norm) to the data within a proper range centered at the local extremes, providing the polynomial coefficients a_k and b_k . Beyond the fact that this procedure enables *a posteriori* error estimate, it may also diminish the unfavorable influence of measurement noise. Second and third degree approximations ($n = 2, 3$) were tested to determine their fit to the theoretical curve given by equation (8) around the extremes. The effect of approximation errors turns out to be insignificant as long as those can be reduced by proper selection of the fit interval. The differences are well below 1 nm s^{-2} if data only within a sufficiently small surrounding of the local extremes (figure 3) are used. The differences

$$\delta g = \text{extr}(\hat{g}_n) - \text{extr}(\tilde{g}) = \hat{g}_n(\hat{l}_{\text{extr}}) - \tilde{g}(\tilde{l}_{\text{extr}}), \quad (11)$$

where $\text{extr}(\hat{g}_n)$ is the value of the local extreme at \hat{l}_{extr} defined by the fitted polynomial approximation, are of the same order (table 1).

Although the favorable effect of a short fitting interval is clear, tests with real observations show that optimum

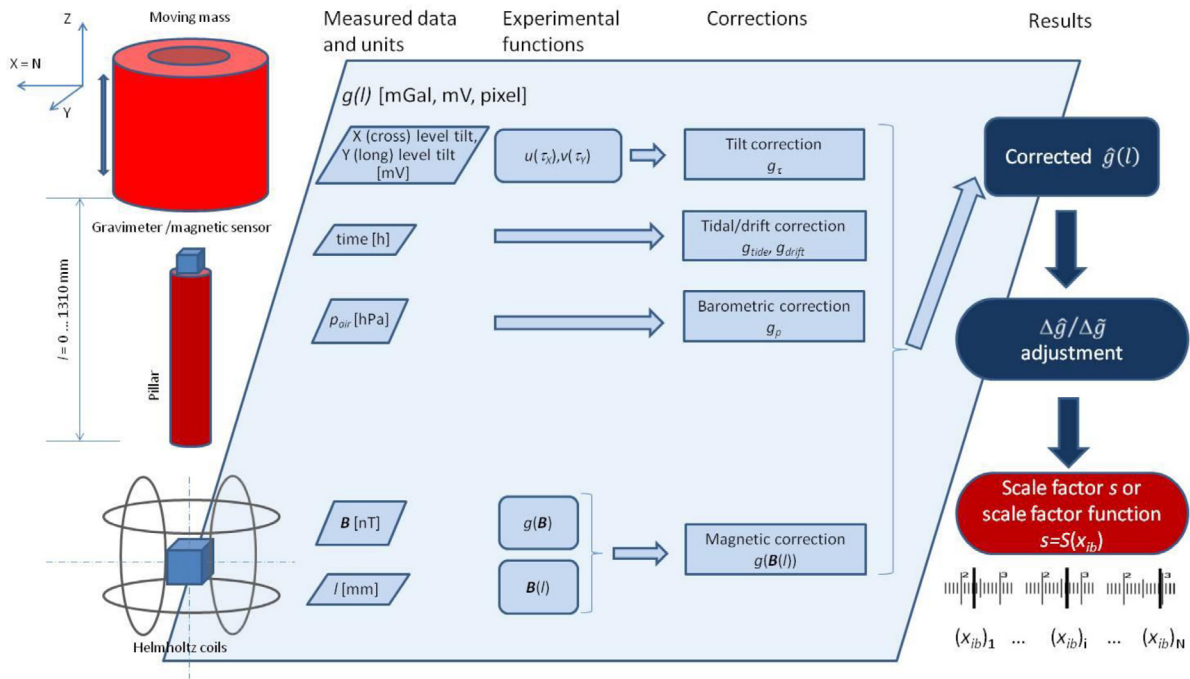


Figure 1. Flowchart of the MMC.

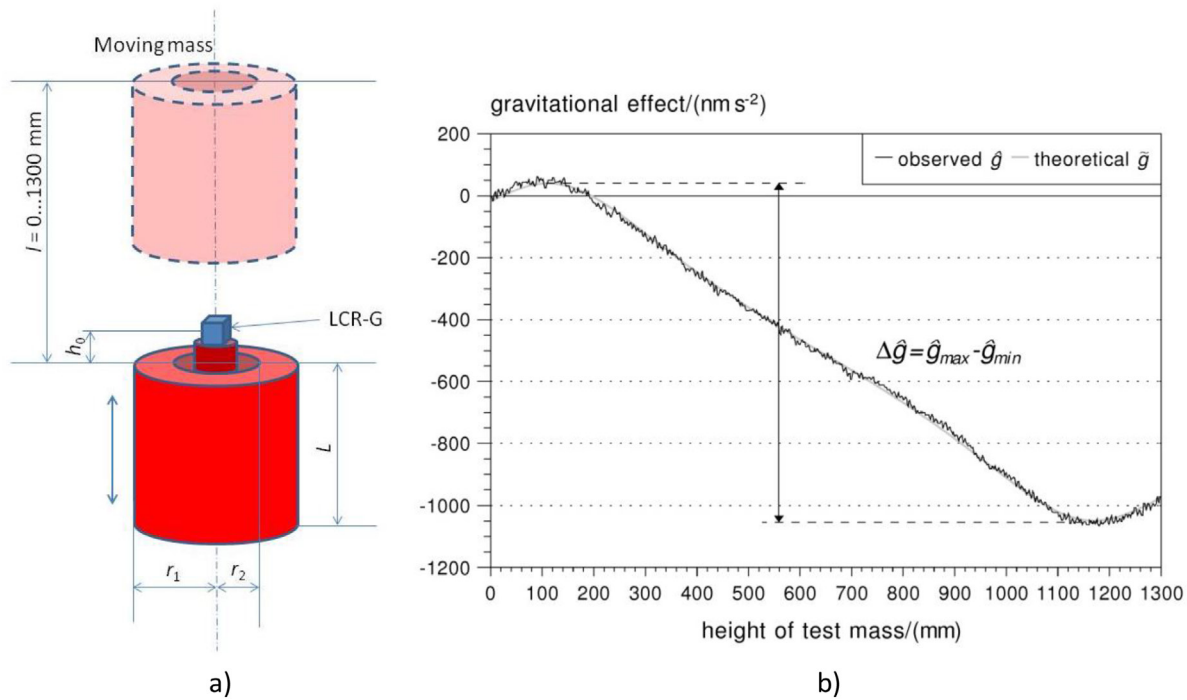


Figure 2. (a) The explanation of the symbols r_1, r_2, h_0, L and l_i in (8). (b) Graphical representation of *Max-Min* and *Full-Fit* methods. Observations are given in nm/s^2 unit and taken from calibration tests done by G1188 providing a scale factor close to 1 (see Section 6).

configurations have to be found experimentally because the interval length cannot be arbitrarily decreased due to the influence of observation noise. Its RMS is around $\pm(10-20) \text{ nm s}^{-2}$ on a silent day or even higher due to strongly weather dependent microseismic activity (Papp et al 2012). So, one needs a sufficiently broad fitting interval (including typically 100–200 observations if 1 Hz sampling rate is applied) in order to obtain reliable local extremes. The limits of the interval, however, should be fixed in the range $(-190 \text{ mm} \leq \tilde{l}_{max} \leq 160 \text{ mm}$

approximately) defined by the two inflexion points preceding and following either the local maximum or the local minimum of the reference signal where it is concave or convex, respectively (figure 3). Consequently the expected internal accuracy of the *Max-Min* method is about $\pm 0.5 \text{ nm s}^{-2}$ for LCRs.

The site noise, however, is much less damped in case of CG-5 gravimeters, depending on the length of the integration period of data measured with 6 Hz internal sampling rate. Arbitrary repeat cycle can be defined for restarting data

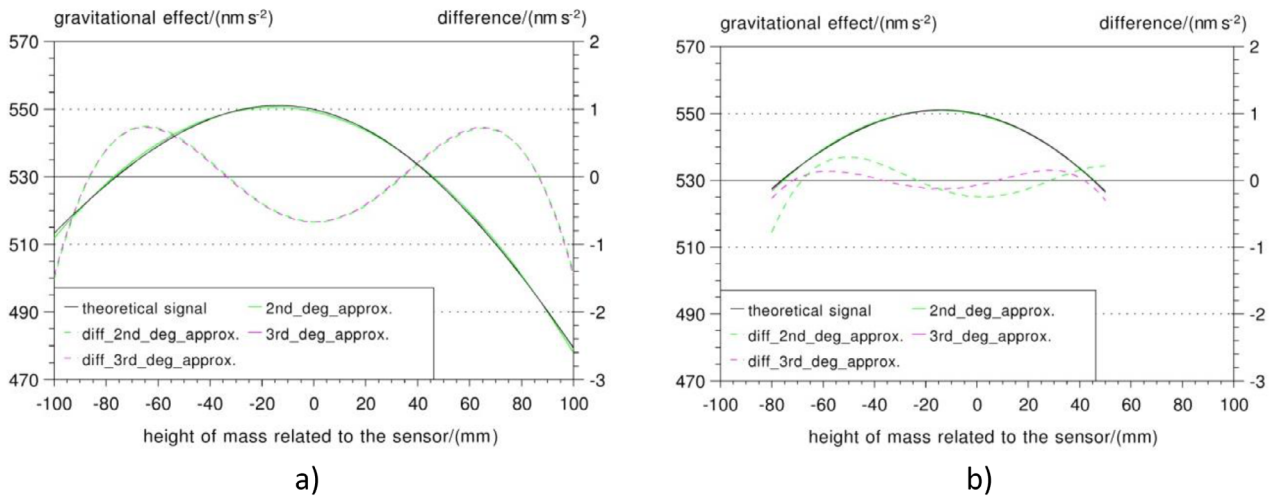


Figure 3. Approximation of the theoretical signal by polynomials around its maximum in height intervals of (a) $-100\text{ mm}-100\text{ mm}$ and (b) $-80\text{ mm}-50\text{ mm}$. The sign of differences is defined by (11).

Table 1. Statistics and results of the L2 norm fitting of $n = 2$ and $n = 3$ degree polynomials to the theoretical gravitational change given by equation (8). The theoretical minimum value $\tilde{g}_{\max} = 551.07\text{ nm s}^{-2}$ at $\tilde{l}_{\max} = -13.9\text{ mm}$. μ_0 is the standard deviation of unit weight observable. δg is defined by (11).

Interval	$n = 2$				$n = 3$			
	\tilde{l}_{\max} mm	$\max(\hat{g}_n)$ nm s ⁻²	μ_0	δg nm s ⁻²	\tilde{l}_{\max} mm	$\max(\hat{g}_n)$ nm s ⁻²	μ_0	δg nm s ⁻²
$-100\text{ mm}-100\text{ mm}$	-15.57	550.56	0.58	-0.51	-15.51	550.55	0.58	-0.52
$-80\text{ mm}-50\text{ mm}$	-14.94	550.94	0.24	-0.13	-13.83	550.94	0.12	-0.13

sampling in regular time intervals. A few seconds are required between the cycles for internal data processing and storage. Typical RMS errors are $\pm(20-40)\text{ nm s}^{-2}$ for 54 s averaging periods and up to more than $\pm 200\text{ nm s}^{-2}$ for 2 s periods. This requires selecting broader fitting intervals which may bias the extreme determination. However, in this case, low-degree polynomials do no longer approximate the theoretical and observed signal within the fit interval with sufficient accuracy; they are not able to capture the true extrema due to smoothing, which leads to an underestimation of the max-min difference. This applies equally to both theoretical and observed data. Therefore, we determine the max-min difference of the reference signal by the same procedure as applied in case of observed data. Within the fit intervals, we select theoretical data samples just at the observed mass positions and adjust polynomials of same degree as for the observations.

The *Full-Fit* method is an extension of the *Max-Min* method since it applies L2 norm fitting not only locally but on the full observation segment recorded during the mass movement. The fitting process provides the optimum estimate of the parameter set (s, h_0, g_0) based on (6) in the observation range $(\hat{g}_{\min}, \hat{g}_{\max})$. Eventually, the solution of equation (6) adjusts equation (8) to the observations by scaling and translation.

In practice the same data sets recorded by the acquisition systems at e.g. 1 Hz sampling rate during the movement of the test mass can be used in both methods for the calibration of LCR gravity meters. So it is optional if the full data set (*Full-Fit* method) or just parts of it around local extrema (*Max-Min* method) are involved in the computation of the scale factor.

In order to check the effect of noise and its influence on the results of *Max-Min* and *Full-Fit* methods simulated data sets composed of the synthetic signal and noise ε with both normal $\varepsilon \in N(0; 15)$ and uniform $\varepsilon \in U(-26, 26)$ distributions were processed. Table 2 shows that *Max-Min* method gives slightly larger scale factors than what is provided by the *Full-Fit* method, which is in a good accordance with the negative differences given by (11) and listed in table 1. If $\delta g(\tilde{l}_{\max}) < 0$ and due to symmetry $\delta g(\tilde{l}_{\min}) > 0$ then the difference $\Delta\hat{g} = \hat{g}_{\max} - \hat{g}_{\min} \cong \max(\hat{g}_n) - \min(\hat{g}_n) = (\tilde{g}_{\max} + \delta g(\tilde{l}_{\max})) - (\tilde{g}_{\min} + \delta g(\tilde{l}_{\min})) = \Delta\tilde{g} + (\delta g(\tilde{l}_{\max}) - \delta g(\tilde{l}_{\min})) < \Delta\tilde{g}$. So the scale factor estimated by (5) is greater than 1. In order to check how a disturbing systematic signal (see section 6.1.2) not modeled in the right hand side of equation (6) but hidden in the observations can bias the parameter estimation simulation data composed of the synthetic and a disturbing signal having average amplitude \bar{A}_{signal} was also processed. The results in table 2 clearly show that the tendentious relation $S_{\text{Max-Min}} > S_{\text{Full-Fit}}$ may reverse whereas the value of $S_{\text{Full-Fit}}$ remains almost unchanged indicating the robustness of the *Full-Fit* method in case of realistic disturbing signals discussed in section 6.1.2.

Different data acquisition schemes, however, are required for Scintrex CG-5 gravimeters as commercial CG-5s do not provide an analog output signal. As it was mentioned above averaging is necessary to diminish the dispersion of a single CG-5 observation. Averaging the 6 Hz samples over 54 s periods enables taking measurements with 1 min sampling

Table 2. L2 norm estimations of parameters s, g_0, h_0 introduced in (6) using simulated (noiseless and contaminated by noise and disturbing signal) calibration data. N and U stand for noise sets having normal and uniform distributions, respectively. The description of disturbing signal is given in section 6.1.2. The reference parameters: $s_0 = 1, g_0 = 600 \text{ nm s}^{-2}, h_0 = 130 \text{ mm}$. Polynomial degree $n = 2$ in *Max-Min* method (see equation (10)). The reference signal was computed from the corresponding parameters (mass, dimensions) of the calibration device described in section 2. The data $g_0, \bar{A}_{\text{signal}}, e_i$ and σ_{noise} are given in nm/s^2 .

Method	Adjusted parameters	Noiseless data	With noise e_i		With disturbing signal	
			$N(\bar{e}_i; \sigma_{e_i})$		$\bar{A}_{\text{signal}} = 5.5$	
			$U(\min_i e_i, \max_i e_i)$	$U(-26, 26)$	Noiseless	$N(0; 15)$
<i>Max-Min</i>	s	1.00097	1.00094	1.00170	0.99269	0.99240
<i>Full-Fit</i>	s	1.00000	0.99982	1.00109	0.99999	0.99981
	g_0	600.00	601.27	599.45	600.81	602.07
	h_0	130.00	130.74	129.73	130.84	131.57

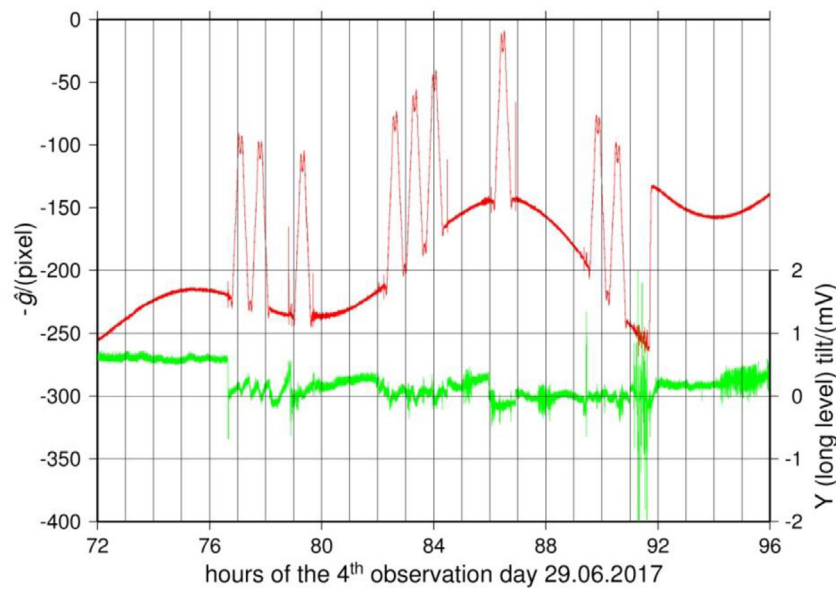


Figure 4. Typical observation day on the 29.06.2017. Calibrated instrument: LCR G949 with electro-optical readout system. The red/black and green/gray curves show the observed gravity change and the long level (Y) tilt, respectively. $1 \text{ mV} = 2.1 \text{ arcsec}$ tilt. Please note the effort to set Y tilt nearly zero ($\leq 0.1 \text{ mV}$) at the beginning of each experiment and the *in situ* test to determine the tilt sensitivity of the instrument (Papp et al 2018) between hours 91 and 92. The micrometer was reset right after this test.

which provides only a few data collected during the continuous upward and downward movement (ca. 2×15 data during $2 \times 15 \text{ min}$ depending on the speed of movement) of the test mass. Therefore, in case of CG-5 experiments, the mass is moved rather stepwise and kept at constant height during 3 min intervals. Only those observations are used, where the mass did not move during the integration period. In this way an arbitrary number of observations can be provided theoretically but taking the increasing uncertainties (environmental effects, tidal model, instrumental drift, etc...) caused by the increasing measuring time into account an optimal configuration of timing of the measurements has to be found.

When operating the CG-5 in continuous recording mode providing time series for *Full-Fit* method the averaging period of the 6 Hz samples was selected by 2s. 2s averages have been taken during the upward and downward movements of the mass for determining the mass position as well.

For LCR gravity meters without feedback system, the derived scale factor s is defined by equation (1). Consequently,

by taking the data series $g(l)$, a suitable average index beam position (either in pixel or mV units) has to be determined from the sample set of observations (figure 4)

$$\bar{x}_{ib} = M\{g\} = \frac{\sum_{i=1}^N g(l_i)}{N} \quad (12)$$

to investigate the scale factor change in the range of the free movement of the beam. The value of N depends on the length and the speed of movement (typically 1300 mm and 1.2 mm s^{-1} , respectively) and the sampling rate (1 Hz). So, the gravitational signal (8) is represented by about 1125 samples per upward or downward movement.

The basic requirement for both methods is that the observed gravity changes reflect only the gravitational effect of the moving mass. Instrumental drift, tides and environmental effects like instrumental tilt and air pressure variation must not ‘contaminate’ the observations. In practice, of course, it is impossible to fulfill this requirement. However, if one restricts the time of calibrations to those periods where

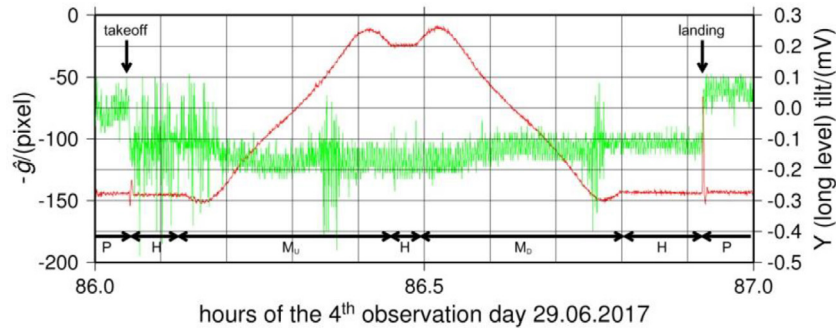


Figure 5. Typical stages of the calibration process and its effect on observed gravity (red/black) and instrumental tilt (green/gray). Calibrated instrument: LCR G949 with electro-optical readout system. 0.1 mV = 0.21 arcsec tilt. P—parking position, H—hanging position, M_U —upward movement of the mass, M_D —downward movement of the mass. Note the reversed sign of the observed gravity change.

the tidal signal is nearly linear within a sufficient tolerance interval, then a common linear model determined from the observations can be used to remove both instrumental drift and tidal signal. For example, if the maximum non-linear tidal (peak-to-peak) contribution is limited to 5 nm s^{-2} , then time intervals of 30–40 min and 80–120 min around maximum/minimum tides and inflexion points, respectively, can be selected. At least 9–10 experiments can be done during a day in the selected time slots, dominantly depending on the phase relations of the main tidal constituents (figure 4). The micrometer of the LCR without feedback system has to be adjusted to scan the whole measuring range (about $10 \text{ } \mu\text{m s}^{-2}$) where the index beam freely moves and a correct determination of its position (e.g. by evaluating CCD images) is possible. The same procedure can be applied for instruments using the CPI readout.

During a complete experiment consisting of one upward and downward movement, the tilt τ changes due to ground coupling between the instrument pier and the frame holding the cylindrical mass (figure 5). The largest tilt effects are caused by the initial takeoff and the final landing of the mass from and on three parking bucks (benches) fixed to the floor, respectively. The Mátyáshegy laboratory is located inside a karstic cave system and the instrument pier is isolated from the pier (a concrete foundation block) holding the moving mass device. Both piers stand on the solid limestone basement. Hence, when the parking bucks are unloaded and the frame of the lifting device takes and redistributes the full load, then the stress field deforming the basement rock is changed locally. Consequently the instrument pier is also tilted according to the deformation of the basement rock.

4. Error analysis

4.1. Application of the error propagation law on the formula of the theoretical signal

Knowing the estimates on the accuracy of the dimensions of the cylindrical ring and its mass one can derive the uncertainty of the calibrating signal based on equation (8).

Since the density $\Delta\rho$ cannot be determined directly it is defined as a function of the volume V of the cylinder and the mass difference ΔM between the iron cylinder and the air:

$$\Delta\rho = \frac{\Delta M}{V} = \frac{\Delta M}{\pi L (r_2^2 - r_1^2)}. \quad (13)$$

Replacing $\Delta\rho$ in equation (8) by the mass difference, it reads as

$$\begin{aligned} \tilde{g}(h_0 - l) &= 2G \frac{\Delta M}{L (r_2^2 - r_1^2)} \left(\sqrt{(h_0 - l)^2 + r_1^2} - \sqrt{(h_0 - l + L)^2 + r_1^2} \right. \\ &\quad \left. - \sqrt{(h_0 - l)^2 + r_2^2} + \sqrt{(h_0 - l + L)^2 + r_2^2} \right) \\ &= 2Gf(h_0, l, L, r_1, r_2, \Delta M). \end{aligned} \quad (14)$$

Based on the law of error propagation the variance $\mu_{\tilde{g}}$ of (14) can be estimated analytically if the variances of its uncorrelated variables are known and the partial derivatives of the function f are derived:

$$\begin{aligned} \mu_{\tilde{g}} &= 2G\mu_f, \text{ where} \\ \mu_f &= \sqrt{\left(\frac{\partial f}{\partial h_0}\right)^2 \mu_{h_0}^2 + \left(\frac{\partial f}{\partial l}\right)^2 \mu_l^2 + \left(\frac{\partial f}{\partial L}\right)^2 \mu_L^2 + \left(\frac{\partial f}{\partial r_1}\right)^2 \mu_{r_1}^2 + \left(\frac{\partial f}{\partial r_2}\right)^2 \mu_{r_2}^2 + \left(\frac{\partial f}{\partial \Delta M}\right)^2 \mu_{\Delta M}^2} \end{aligned} \quad (15)$$

provided that all of the parameters $h_0, L, r_1, r_2, \Delta M$ and the variable l are independent of each other. As figure 6 shows the error contribution ε due to the uncertainty μ of the parameter $\text{par} \in \{h_0, L, r_1, r_2, \Delta M\}$ defined as $\varepsilon_{\text{par}} = \sqrt{(\tilde{g}'_{\text{par}})^2 \mu_{\text{par}}^2}$ changes as l changes during the movement of the test mass. The formulae of the partial derivatives (\tilde{g}'_{par}) used in the error propagation analysis are listed in the Appendix.

The total error of the signal provided by equation (15) in figure 6 is a kind of maximum error estimate since some of the error sources can be excluded by a proper calibration method detailed in the following sections. Generally spoken, the most dominant error sources are the uncertainties of the inner and outer radii r_1 and r_2 respectively and that of h_0 . Fortunately the latter has not much contribution around the maximum and minimum places of the calibrating signal which play a prominent role in the calibration process.

4.2. Effect of the systematic error of h_0

Although this problem was already investigated partly in the previous section and partly in the Appendix the estimation given there characterizes only the effect of the non-systematic component in the error budget of the parameter h_0 which is the exact vertical sensor position of the gravimeter.

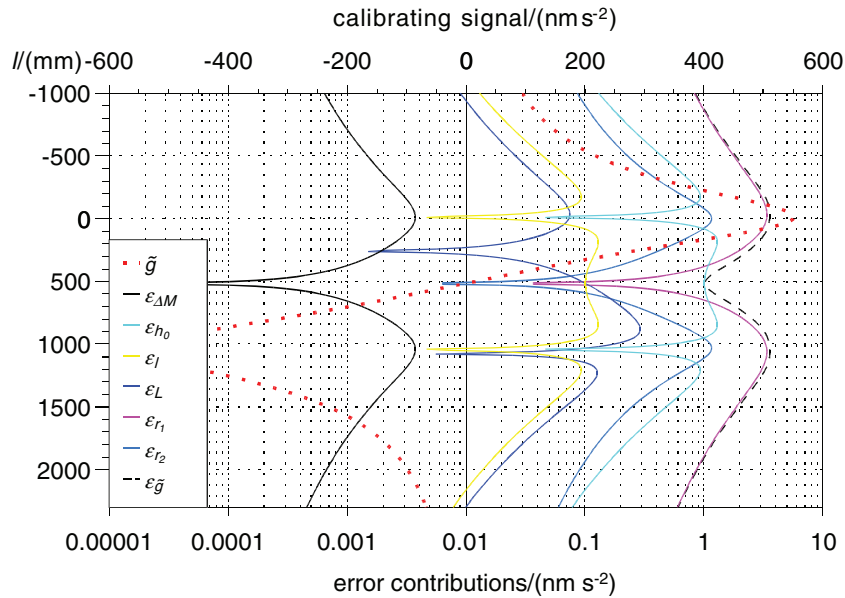


Figure 6. Error contributions from the non-systematic uncertainties of the parameters of the cylindrical ring to the total error (shown by black dashed line) of the calibrating signal (red/black dotted line) as a function of l (height of the top of the cylinder above the reference point of the sensor). $\mu_{\Delta M} = \pm 0.021$ kg, $\mu_L = \mu_{r_1} = \mu_{r_2} = \pm 0.0002$ m, $\mu_{h_0} = \pm 0.001$ m, $\mu_l = \pm 0.0001$ m, $\mu_L = \pm 0.0002$ m.

It is, however, unknown and appears as non-linear quantity in equation (8). Therefore, we have to provide an estimate of the sensor position and introduce its systematic deviation dh from h_0 as unknown in the adjustment process. However, the gravity response to the mass movement is non-linear with respect to dh as well, so that linearization is required by truncating a Taylor series expansion after the linear term. Unfortunately, the misfit of the truncated Taylor series to the exact formulation (equation (8)) correlates with the theoretical signal (figure 7) and hence will produce a systematic bias of the estimated calibration factor (table 3). The bias depends on dh . Therefore it is important to estimate the sensor position h_0 as exactly as possible or to solve this problem by an iterative adjustment approach. Subsequent iterations let h_0 converge to a value which minimizes the bias of other parameters being estimated.

4.3. Effect of the eccentricity of gravimeter sensor

Due to mathematical difficulties this specific effect cannot be investigated by the method provided by error propagation law. Since closed analytical formula of the gravitational field of the cylinder exist only for points located on its vertical axis, the effect of eccentricity of the gravimeter sensor mass related to the vertical axis was computed from a model of cylindrical ring mass approximated by special polyhedral volume elements (right triangular prisms) with the same height as of the cylindrical ring (figure 8). The triangular bases are approximately isosceles triangles, the total number of which was 21600. This provides an approximation accuracy of first derivatives of the gravitational potential (Benedek 2016) in the inner and near area of the cylindrical ring better than 10^{-2} nm s^{-2} . This method was used to calculate the gravitational effect in off-axis points shown in figure 8, where the horizontal sensor displacement varied between 0 mm and 50 mm

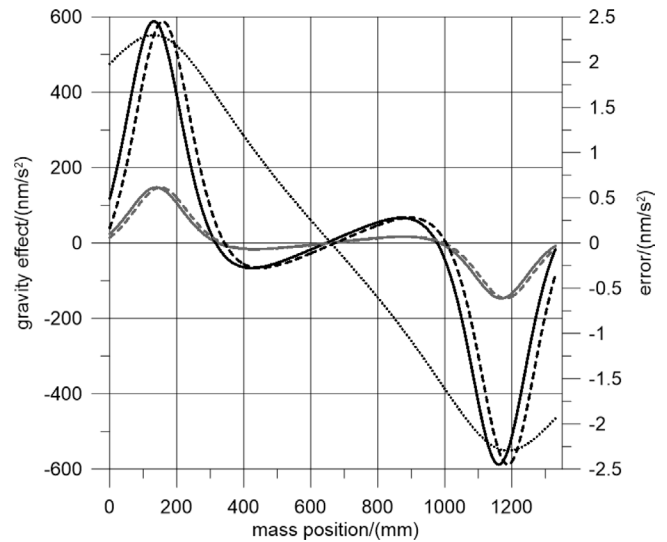


Figure 7. Misfit (i.e. the quadratic and higher order terms in the Taylor series expansion) of the linearization approach for $dh = +10$ mm (light gray solid line), $dh = -10$ mm, (light gray dashed line), $dh = +20$ mm (black solid line), $dh = -20$ mm, (black dashed line). Dotted black: theoretical signal.

Table 3. Regression coefficient of the gravity effect represented by a truncated Taylor series versus exact gravity effect based on equation (8).

dh/mm	+10	-10	+20	-20
Regression coefficient (linear approx. versus theoretical effect)	1.00056	1.00056	1.00223	1.00224

in 10 mm steps. Due to cylindrical symmetry 2D horizontal displacements can be simplified to radial displacements.

Knowing the inner structure of the sensor boxes of both LCR and CG-5 gravity meters and the limited possibility of

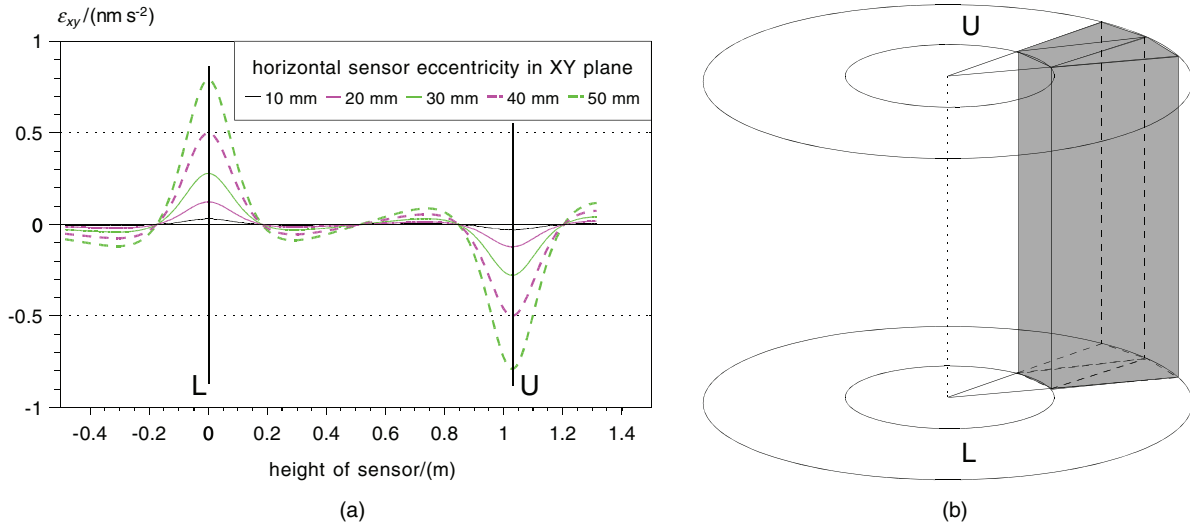


Figure 8. (a) The effect of the horizontal eccentricity of the gravimeter sensor ε_{xy} as a function of its vertical position measured from the lower plane (L) of the cylindrical mass. ε_{xy} is determined for five different radial offset values (see the embedded legend). The thick vertical lines at 0 m and 1.03 m show the position of the lower (L) and upper planes (U) of the cylindrical mass, respectively. (b) The sketch of the approximation of the cylindrical ring by polyhedrons which were applied in the determination of ε_{xy} .

the horizontal positioning of the gravity meters inside the inner ring of the cylinder the sensor mass eccentricity is certainly much less than 50 mm. Consequently the error due to sensor mass eccentricity is much less than 1 nm s^{-2} . Probably it is around 0.1 nm s^{-2} .

5. Corrections of the observations

As already indicated in section 2, different standard (tidal, drift, barometric) and non-standard (tilt, magnetic) corrections (figure 1) have to be applied on the raw gravity data during the data processing:

$$\hat{g} = g(t) - g_{\text{drift}}(t) - g_{\text{tide}}(t) - g_{\tau}(t) - g_p(t) - g(B). \tag{16}$$

5.1. Standard corrections

5.1.1. Barometric correction. Barometric corrections were computed from the differences between normal and measured atmospheric pressure p by applying the single admittance concept (U.S. Standard Atmosphere 1976):

$$g_p = 3 \cdot (p_{\text{air}} - 1013.25 \cdot (1 - 0.0065 \cdot H/288.15)^{5.2559}) \text{ (nms}^{-2}\text{)} \tag{17}$$

where p_{air} is the observed air pressure (hPa), and H is the instrument elevation (m). This effect results typically in a correction of a few nm/s^2 during a calibration cycle while its error $\mu_{g_p} < 1 \text{ nm s}^{-2}$ according to the accuracy ($\mu_p = 0.1 \text{ hPa}$) of the barometer used.

5.1.2. Tidal and drift correction. In the case of LCR gravimeters, it was assumed that drift and tides are sufficiently linear during a complete mass movement cycle (up and down, duration ~ 30 min) when experiments are scheduled to epochs of local extrema and inflexion of the tidal variation (figure 4). In practice it means that with careful selection of the observation

periods non-linear tidal residuals remain in the range of $\pm(2 - 3) \text{ nm s}^{-2}$. The combined effect (tidal and drift) was corrected by subtracting a straight line (defined by the parameters \hat{g}_0 and m) adjusted to the data acquired during hanging periods (figure 5) before and after a complete movement cycle:

$$g_{\text{drift}}(t) + g_{\text{tide}}(t) = g(t) - g_{\tau}(t) - g_p(t) = \hat{g}_0 + mt, \tag{18}$$

where time t is also recorded. Applying (18) in (16) one obtains reduced observations \hat{g} reflecting only the gravity field variation caused by the moving mass.

Alternatively, tides can be predicted based on precise tidal models if available as for the Mátyáshegy site. Tidal residuals, if present, can then be modelled together with the instrumental drift by low-degree polynomials, even in an iterative process. This approach has been used for the CG-5 experiments in both calibration methods. The commonly strong instrumental drift of the CG-5 has been adjusted by considering all repeated observations at the different mass positions similarly as done in conventional field surveys. For the astatized and feed-back-less instruments this method, however, cannot be applied due to the unknown scale factor function which makes the computation of the measured tidal effect at an arbitrary index beam position x_{ib} impossible with the required accuracy.

5.2. Non-standard corrections of observations

5.2.1. Magnetic effect of the mass. As the calibration mass is made of steel, its magnetic effect significantly modifies the Earth’s magnetic field where the instrument is set up during the experiments. Practically the magnetic field of the Earth almost disappears inside the cylinder near to its centre of mass. This was already revealed earlier and it was one of the main objections against the facility. Though presumed it was neither considered nor discussed up to now.

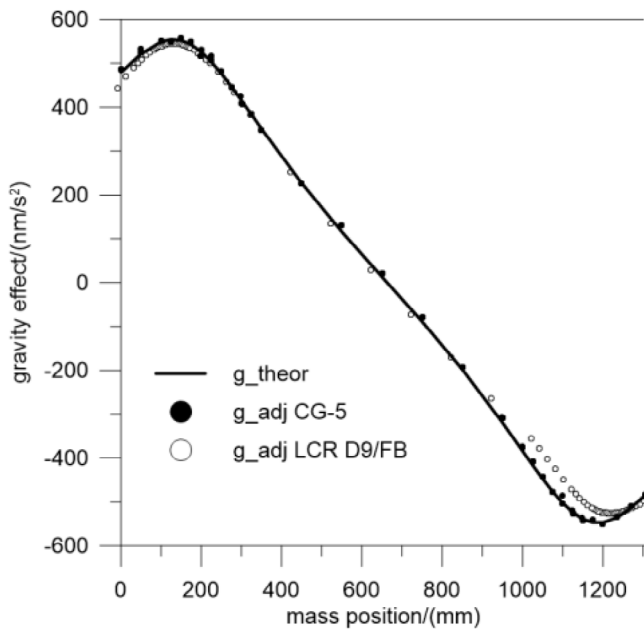


Figure 9. Comparison of adjusted gravity response of CG-5 SN#40236 (December 2017) and LCR D-9/SRW-FB (1994 and 1995) with the theoretical signal.

The magnetic effect must be corrected for, at least for metal spring gravimeters; otherwise, the scale factors may be strongly biased. An early experiment with LCR D9/Feedback SRW-D (Schnüll *et al* 1984) in 1994 and 1995 was re-evaluated proving the strong distortions due to this effect. The feedback of LCR D-9 was carefully calibrated before the experiments on the Hannover calibration line (Kanngieser *et al* 1983). The scale factor bias was 2%–3% due to a systematic deviation of observed gravity from the theoretical signal. Figure 9 compares the adjusted response of different gravimeters and the theoretical gravity variation. While the CG-5 response closely follows the theoretical gravity effect, the LCR deviates remarkably, when the mass is in up-position. It is assumed that this is caused by the magnetic effect of LCR D-9.

It is not simple at all to measure the magnetic effect of such an enormous steel-mass. The geomagnetic instruments generally used in observatories and at field works are useless in this case. The vector magnetometers are measuring the variation of geomagnetic field with high accuracy (sub-nT) but in a very narrow range (few μT only). Scalar magnetometers are able to measure the required measuring range but do not provide direction information. Therefore the new FluxSet magnetometer (figure 10(a)) was tested, which measures the magnetic field strength in three perpendicular spatial directions simultaneously. The total maximum magnetic effect of the calibration mass (figure 10(b)) is about 48 μT and exceeds significantly the magnitude of Earth's magnetic field. It was also measured by two Honeywell HMC5983 magnetic sensors calibrated in Helmholtz coils *a priori*. The results of both instrument types are the same. Consequently, the LCR instruments containing metal springs are certainly influenced by this effect exerting a disturbing non-gravitational force (Torge 1989, Pálinkáš *et al* 2003).

The response of gravimeters to magnetic forces was determined experimentally in a Helmholtz coil following the scheme given by Pálinkáš *et al* (2003). During the tests the excited magnetic induction field components B_x , B_y and B_z in directions X (cross level), Y (long level) and the vertical respectively, varied between -80 to $+80$ μT with steps of 10 μT (figure 11). The magnetic induction and its effect on gravimeter readings were registered with 1 Hz sampling rate. Based on (1) the accuracy of the FluxSet magnetometer measurements ($\mu_B = B/100$) defined by its technical specifications and (2) the error propagation analysis of the magnetic sensitivity functions (which are sufficiently linear in the field interval between -40000 nT and 40000 nT) the error of the magnetic correction (e.g. in x direction) is given:

$$\varepsilon_{B_x} = \sqrt{(\mu_a)^2 + (\mu_b)^2 B_x^2 + (\mu_{B_x})^2 b^2}. \quad (19)$$

In (19) a and b are the parameters of the linear sensitivity model ($g(B_x) = a + bB_x$), μ_a , μ_b , μ_{B_x} are the *a posteriori* standard deviations of the adjusted model parameters a , b and the measured magnetic field component B_x , respectively. In the case of LCR G949 the largest influence of the magnetic field on the readings is in y direction (figure 12(b)). The estimated error contribution of the B_y field component ε_{B_y} is 0.21 pixel (≈ 1.6 nm s^{-2}) using the following parameters: $a = 0.1973$ pixel, $b = -0.0002086$ pixel nT^{-1} , $B_y = 40000$ nT, $\mu_a = 0.11484$ pixel, $\mu_b = 0.00000376$ pixel nT^{-1} and $\mu_{B_y} = 400$ nT. Regarding the sensitivity functions in figure 12 the maximum uncertainty of the magnetic corrections is probably less than 2 nm s^{-2} .

Figure 12 presents the magnetic sensitivity $g(\mathbf{B})$ of the LCR G instruments in three directions. The response to magnetic field variations is different for each instrument and strongly depends on the direction.

Based on these sensitivity functions, corrections for the magnetic effect of the moving steel-mass can be calculated for each instrument individually (figure 13). If e.g. a linear approximation is used to model the magnetic response of a gravimeter for all 3 components then the field variation measured inside the cylindrical ring mass (figure 10(b)) can be converted to reading corrections. The magnetic effect biasing the gravity observations may vary in a range of ± 70 nm s^{-2} depending on the instrument (figure 13).

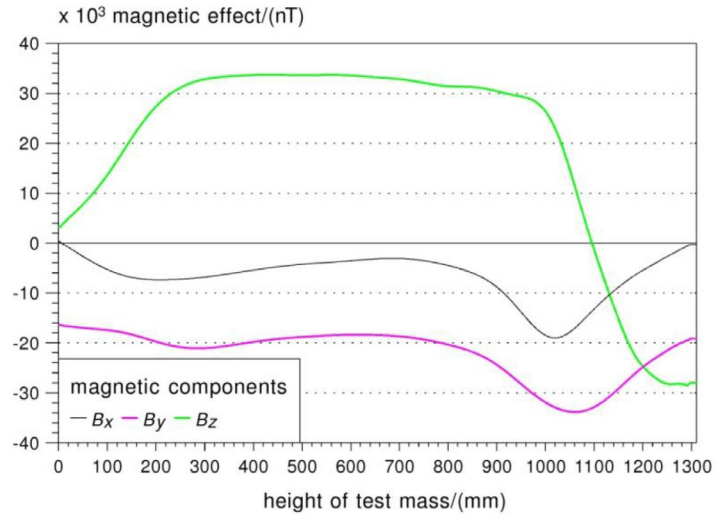
5.2.2. Tilt corrections. Based on the paper by Riccardi *et al* (2009), the tilt sensitivity, i.e. the response of LCR G meters to unit tilt at a given index beam position x_{ib} , was determined as described by Papp *et al* (2018). However, one should note that the tilt sensitivity in Y (long level) direction investigated in the latter paper is more complex (due to the astatized sensor characteristics) than just the simple geometrical relation

$$g_\tau = g \cdot (1 - \cos(\tau)) \quad (20)$$

causing negligible differences ($|g_\tau| \approx 10^{-8}$ nm s^{-2}), if e.g. $g = 1000$ nm s^{-2} and $|\tau| \leq 2$ arcsec hold. This condition for τ can be easily provided during an experiment (figure 5) so the determination of the tilt sensitivity function only in Y (long level) direction is sufficient. In X direction (20) can be used but

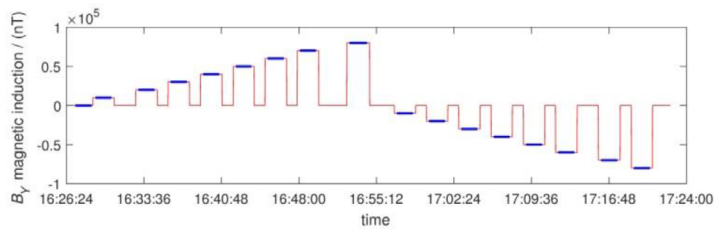
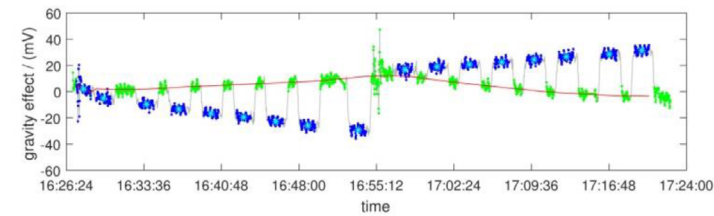


a)

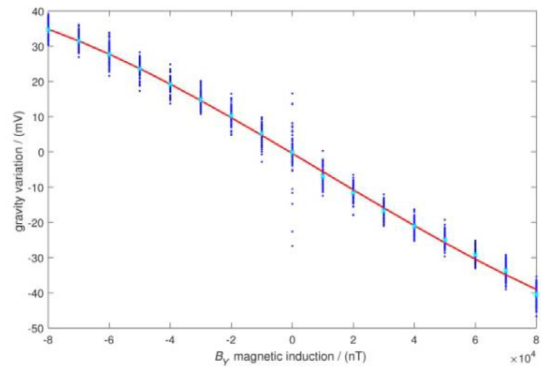


b)

Figure 10. (a) FluxSet magnetometer on the top of the instrument pillar of the calibrating device, (b) magnetic effect of the moving mass.



a)



b)

Figure 11. (a) Raw data series of LCR-G 220 with induced magnetic field variations in Y (long level) horizontal direction. (a) The green/light gray and the blue/dark gray curves on the upper chart show the readings during zero and non-zero induction B_y , respectively. (b) Magnetic sensitivity function of LCR-G 220 in Y direction.

it has no significant effect on the readings. Since the output signal of the LCR levels are given in mV unit, the instrument dependent factors to convert mV unit to arcsec were determined by a spirit level balance device of the Geodetic and Geophysical Institute MTA CSFK with an accuracy of 0.1 arcsec.

For those LCR instruments which are not equipped with feed-back system (G220, G949, G963) the effect of tilt (supposed that $|\tau_y| < 2$ arc sec) on the gravity readings may reach even more than 100 nm s^{-2} when the index beam is close to the limiters of the free movement range. For G1188 the effect is negligible since the beam stays always around the tilt insensitive position (reading line) in case of proper instrument adjustment. As figures 4 and 5 show, the tilt τ can be kept easily in the interval $|\tau| \leq 2$ arcsec ≈ 0.93 mV in each direction if the levels are set to (nearly) zero before each experiment.

Equation (19) can formally be used to estimate the error of the tilt corrections $\varepsilon_{g_{\tau_y}}$ since the tilt sensitivity (as the function of x_{ib}) is linear (Papp et al 2018):

$$\delta g_{\tau_y}(x_{ib}) = a + bx_{ib}. \tag{21}$$

It gives the response of the gravimeter to unit tilt at a given index beam position. The following parameters derived from almost 900 tilt experiments done for the determination of the tilt sensitivity function of LCR G949 gravimeter can be used first to estimate the accuracy of tilt sensitivity $\mu_{\delta g_{\tau_y}}$: $a = -2.6586 \text{ pixel mV}^{-1}$, $b = -0.0323 \text{ mV}^{-1}$, $\mu_a = 0.16222 \text{ pixel mV}^{-1}$ and $\mu_b = 0.00041 \text{ mV}^{-1}$. Substituting B_x with x_{ib} and μ_{B_x} with $\mu_{x_{ib}}$ and letting $x_{ib} = 700$ pixel as the maximum value of index beam position and $\mu_{x_{ib}} = 1$ pixel in (19), one obtains that $\mu_{\delta g_{\tau_y}} = 0.33125 \text{ pixel mV}^{-1}$ as the

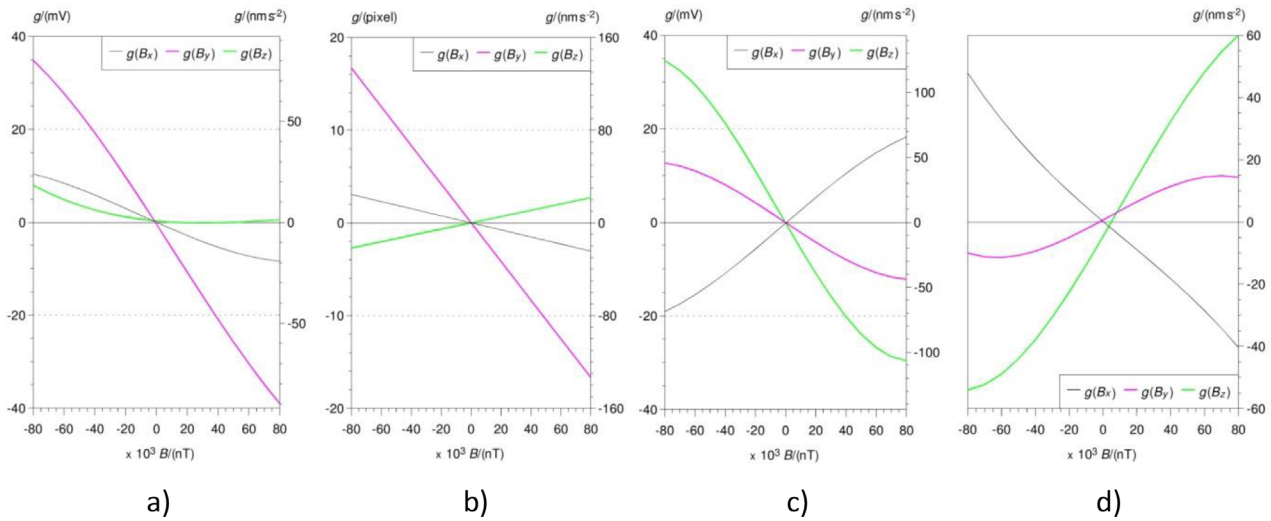


Figure 12. The magnetic sensitivity of LCR G gravimeters, determined using Helmholtz coils. Instruments: (a) LCR G220, (b) LCR G949, (c) LCR G963 and (d) LCR G1188.

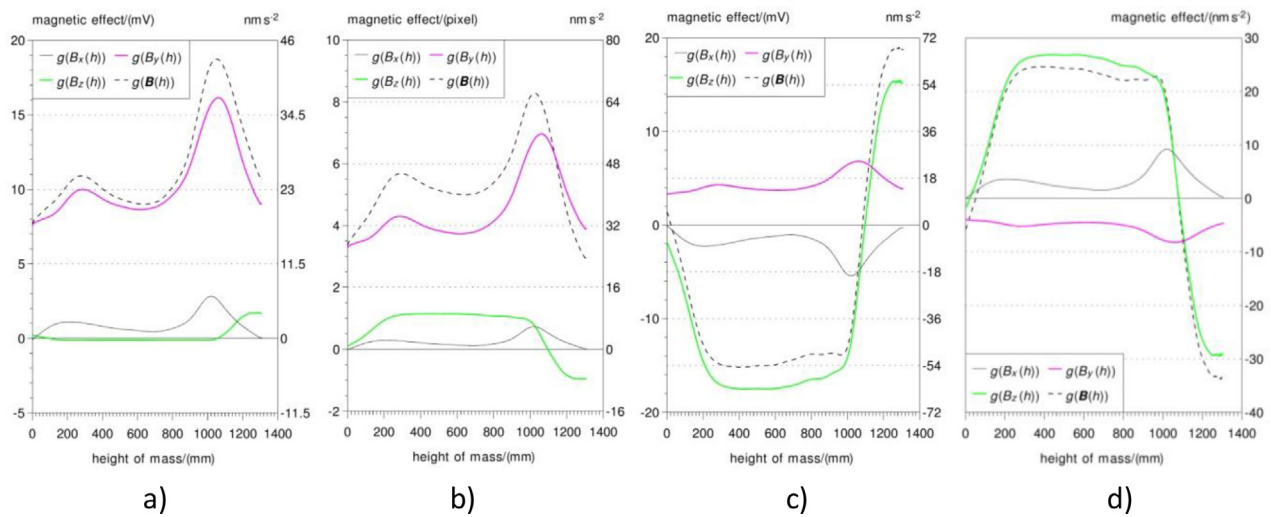


Figure 13. Correction for the magnetic effect of the moving mass, based on the individual magnetic sensitivity functions of LCR G gravimeters. The total effect of the magnetic variation on readings is represented by the dashed black lines on each sub chart. Instruments: (a) LCR G220, (b) LCR G949, (c) LCR G963 and (d) LCR G1188.

maximum uncertainty of the tilt sensitivity value. Since the tilt is limited as it was discussed above the error is defined as $\varepsilon_{g\tau_y} = \max(\tau_y) \mu_{\delta g\tau_y} = 0.93 \mu_{\delta g\tau_y} \leq 0.3 \text{ pixel} \approx 2.4 \text{ nm s}^{-2}$. Figures 4 and 5 however show that the accuracy is usually higher since the tilt τ_y is only a fraction of 0.9mV (around $\pm 0.2 \text{ mV}$) during a calibration cycle therefore the error of tilt correction is probably less than 1 nm s^{-2} .

For CG-5 gravimeters, tilt is observed and automatically corrected for by the internal data processing.

6. Calibration results

6.1. LCR G gravimeters

6.1.1. Comparison of results obtained by Max-Min and Full-Fit methods. Five LCR G meters were tested in the calibration device at different micrometer settings doing 5–11

mass movement cycles each day. The calibration range was $\sim 10 \mu\text{m s}^{-2}$ in case of LCR G949 (optical reading), $\sim 6 \mu\text{m s}^{-2}$ in case of LCR G220 and G963 (CPI) and $200 \mu\text{m s}^{-2}$ in case of LCR G1188 (with feed-back). Table 4 shows the total number of mass movement cycles (1 cycle = 1 up and 1 down movement) for the individual instruments.

During the tests, the gravity reading g_i , the long (Y) and cross (X) level data $(\tau_y)_i$ and $(\tau_x)_i$ respectively, the instantaneous moving-mass height l_i , the air pressure p_i and UTC time were recorded at 1 Hz sampling frequency.

The scale functions depending on the index beam position x_{ib} were determined by both the *Max-Min* and the *Full-Fit* method for each gravity meter (figure 14). As expected, the scale factors of instruments equipped with CPI or CCD ocular strongly depend on x_{ib} , while the scale factor of LCR G1188 equipped with ALIOD-100 feed-back system is constant within the accuracy of the calibration measurements.

Table 4. Time table of calibration experiments.

Instrument	Date	Nr of cycles
LCR G949 (optical)	A: 09 July–22 July 2013	64
	B: 23 April–30 April 2014	56
	C: 29 March–04 April 2016	58
	D: 26 June–03 July 2017	67
LCR G220 (CPI)	27 October–31 October 2014	38
LCR G963 (CPI)	04 August–10 August 2015	43
LCR G1188 (ALIOD 100 FB)	17 February–01 March 2016	71
CG-5 S/N 070340236	04 December–06 December 2017	16

In case of instruments with CPI, significant anisotropy is indicated depending on the direction of the mass movement (figure 14). The scale functions resulting from the two processing methods show slight differences too for all the investigated instruments. The *Max-Min* method gives systematically higher scale factors than that of the *Full-Fit* method which is a consequence of the different characteristics of local and global adjustments of the observations to a part or the whole of the reference signal (8), respectively.

The *Full-Fit* method utilizing a common L2 norm adjustment allows for assessing both the overall calibration accuracy and the reliability of the adjusted parameters involved in equations (6)–(8) (table 5). The most important quantity among them is the average standard deviation (SD) μ_s of the scale factors ($s = k^{-1}$) determined from each single cycle of moving mass experiment (table 5). It clearly shows that the *a posteriori* reliability of the scale factors for most of the tested instrument varies between 0.004 and 0.008 (either in $(\text{nm}/\text{s}^2)/\text{mV}$ or $(\text{nm}/\text{s}^2)/\text{pixel}$ unit, respectively) which means an accuracy of $(1-2) \text{ nm s}^{-2}$ in case of a $500 \text{ mV}/150 \text{ pixel } g$ variation equivalent to about 1100 nm s^{-2} peak-to-peak signal amplitude. LCR G1188 proved to be the best instrument having a firm calibration factor providing 1.3 nm s^{-2} accuracy formally. These results are in good agreement with those derived from the analysis of tidal time series recorded by well-maintained spring gravity meters equipped by feedback system (e.g. Pálinkáš 2006, Papp et al 2018). In favorable conditions the SD of the residuals e_i obtained from conventional tidal adjustment (Wenzel 1996) of the observations are in the range of a few nm/s^2 for records as long as a year at least. Table 6 shows the SD-s provided by the adjustment procedure (6) for both upward and downward directions of the measurement cycles. Based on the SD values of raw data one could conclude that the calibration process cannot provide better overall accuracy than 10 nm s^{-2} in the range of tidal signal. This, however, depends strongly on the environmental noise and is still much better than what can be generally obtained by the spring type gravity meters in field survey applications (typically $\geq 50 \text{ nm s}^{-2}$). It is a clear indication of the favorable laboratory environment ensured by the Mátyáshegy Observatory.

6.1.2. Time- and frequency domain analysis of observation residuals. Residuals computed for LCR G meters show a non-random systematic effect both in upward and downward directions (supplementary material, figure 1 (stacks.iop.org/MET/57/015006/mmedia)). This result, however, could be

difficult to interpret as the influence of (1) any of the error sources discussed in section 4 and/or (2) the imperfection of the applied corrections discussed in section 5. The most probable explanation of this specific characteristic is the rheology of the astatized spring sensors causing delayed response to the relatively quick change of the gravity field induced by the moving mass. Due to the high noise ($\pm 200 \text{ nm s}^{-2}$) at 2 s sampling rate, the CG-5 could not either support or disprove this assumption undoubtedly. No residual signal similar to those of the LCR G meters can be seen (figure 1, supplementary material). This might be expected as CG-5 is a linear, non-astatized gravimeter. Note that the signal shown in the top panel of figure 15 is a modification of $\frac{\partial^2(g)}{\partial t^2}$ by subtracting a linear trend fitted to the second derivatives in the height interval $0 \leq h \leq 1310 \text{ mm}$. It simply equalizes the amplitudes of local peaks (see the ratios of local extrema shown either in figure 7 or 8), consequently it makes the visual comparison easy. A discussion of the frequency content of the residuals is provided in the supplementary material.

6.2. CG-5 gravimeter

Finally, a well-calibrated CG-5 has been used as reference in order to evaluate the performance of the calibration device. CG-5 S/N 070340236 is calibrated twice a year on a vertical calibration line controlled by AG measurements. The scale factor proved to be constant at an accuracy level better than 0.05 per mille so far (Meurers 2018). Using this scale factor CG-5 immediately provides the observations in mGal (10^{-5} m s^{-2}) unit so the value of the scale factor derived from MM calibration is expected to be close to 1.

Figure 16 presents exemplarily the result from the first CG-5 experiment on 2017 12 06. Figure 16(a) shows the adjustment of data within a fit interval centered at the extrema. The solid lines in figure 16(b) display the 3rd degree polynomials locally adjusted to theoretical (black) and observed (gray dashed) gravity sampled at exactly the same mass positions.

Figure 17 presents the results of all experiments. Regarding the *Max-Min* approach (filled circles/triangles in figure 17), experiment 171206_1 is the only one extending over 4 mass movement cycles, all the others covered only one cycle each. The sensor height h_0 used in equation (8) was estimated by about 145 mm. The scale factors differ by a few per mille depending on the way how the extremes of the theoretical signal are determined. Expectedly, the accuracy increases with the number of observations. The scale factor is close to

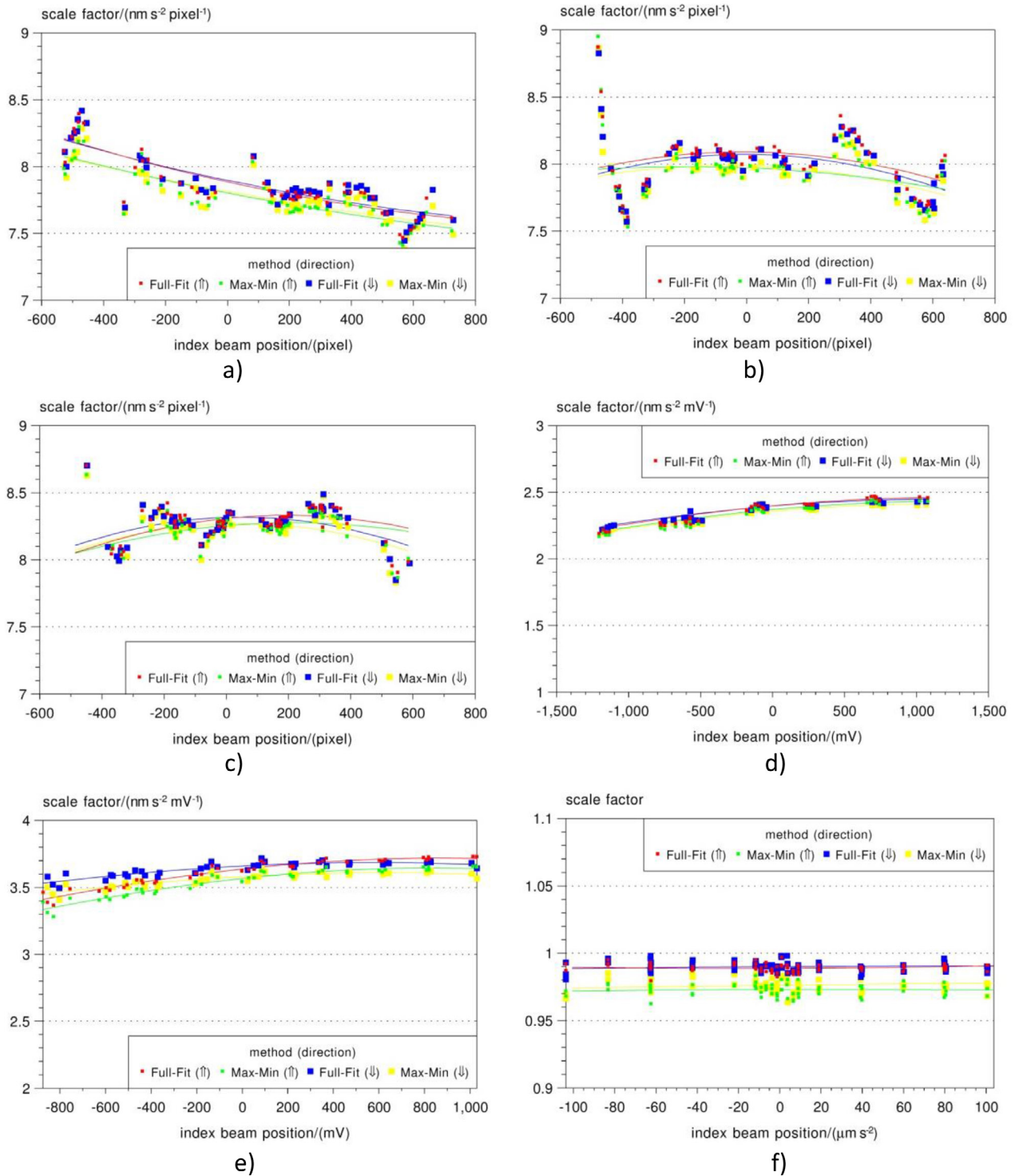


Figure 14. Experimental scale functions of the tested instruments. (a) LCR G949/B, (b) LCR G949/C, (c) LCR G949/D, (d) LCR G220, (e) LCR G963 and (f) LCR G1188.

unity and the overall accuracy is about one per mill. Averaging over repeated experiments will certainly increase this number further.

The CG-5 observations show much higher noise level than the LCR gravimeters do (figure 18). Consequently much broader intervals around the extremes are needed for reliable determination of the extremes in the *Max-Min* approach. A systematic bias of the scale factors can clearly be seen if the

theoretical max-min difference of the reference signal is used (filled triangles in figure 17). Therefore, it is recommendable to determine the max-min difference of the reference signal in the same way as done for observed gravity, i.e. by using theoretical and observed data acquired at exactly the same mass positions (filled circles in figure 17, see also section 3).

The results of the full fit method obviously show much larger uncertainty. This is mainly due to the very high scatter

Table 5. *A posteriori* accuracy estimates of the parameters s , h_0 and g_0 involved in the adjustment model (*Full-Fit* method) of the observations recorded during the calibration campaigns. The data are average values of output results provided by the adjustment of each observation cycle (up and down movement). The fourth column shows the error contribution of μ_s normalized to 1100 nm s^{-2} peak-to-peak signal using a suitable average value \bar{s} of the scale factor.

Instrument (epoch)	Processed cycles	Parameters			
		$\mu_s/\text{scale unit}$	$\mu_s \cdot 1100 \text{ nm s}^2/\bar{s}/(\text{nm/s}^2)$	$\mu_{h_0}/(\text{mm})$	$\mu_{g_0}/\text{reading unit}$
LCR G220	37	0.0036 (nm/s ²)/mV	1.7	0.84	0.36 mV
LCR G949 (B)	46	0.0083 (nm/s ²)/pixel	1.2	0.53	0.07 pixel
LCR G949 (C)	49	0.0083 (nm/s ²)/pixel	1.1	0.57	0.07 pixel
LCR G949 (D)	62	0.0060 (nm/s ²)/pixel	0.8	0.40	0.05 pixel
LCR G963	43	0.0065 (nm/s ²)/mV	2.0	0.98	0.27 mV
LCR G1188	69	0.0012	1.3	0.64	0.07 nm s ⁻²

Table 6. Standard deviations of all the residuals (supplementary material figure 1 (stacks.iop.org/MET/57/015006/mmedia), black dots) obtained from all calibration cycles based on *Full-Fit* method. Corrected residuals represent the residual data after the removal of the average residual signal (supplementary material figure 1 gray lines) which can be sufficiently modeled with a 5th degree polynomial.

Instrument (epoch)	Raw residuals		Corrected residuals	
	SD (upward)/nm s ⁻²	SD (downward)/nm s ⁻²	SD (upward)/nm s ⁻²	SD (downward)/nm s ⁻²
LCR G220	17.04	17.59	15.43	15.71
LCR G949 (B)	12.22	10.56	9.83	8.42
LCR G949 (C)	12.52	10.37	10.36	9.10
LCR G949 (D)	9.27	8.35	7.57	6.67
LCR G963	20.88	18.35	6.60	6.52
LCR G1188	13.02	12.89	9.61	9.94

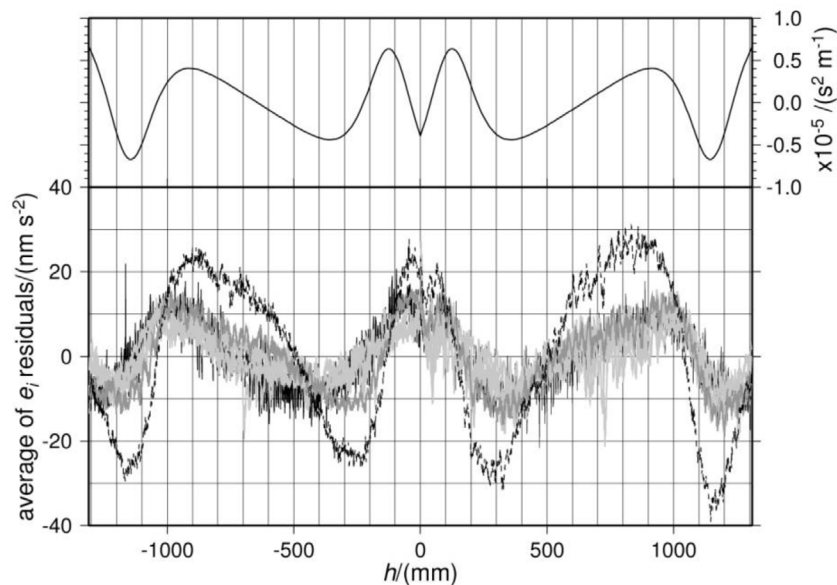


Figure 15. (Top): The black solid line shows the second derivative $\frac{\partial^2(\tilde{g})}{\partial h^2}$ of (8) reduced by its linear trend computed for the interval $0 \leq h \leq 1310 \text{ mm}$. (Bottom): Signals computed as the average of residuals provided by the *Full-Fit* method (6) as a function of mass height. Negative values of h show data for downward direction, therefore top and bottom positions are indicated at $h = +/ - 1310 \text{ mm}$ and $h = 0 \text{ mm}$, respectively.

of the CG-5 observations averaged over periods of as small as 2s, while the experiments using 54s intervals suffer from low sample numbers entering the adjustment procedure (figure 18). Experiment 171206_1 with 54s integration period and >560 observations fits best to the expected scale factor.

For both approaches, the same results with scale factors close to unity were obtained as expected. In particular, this holds for the most reliable experiment 171206_1. The standard deviation of the mean over all experiments is about 7 per mill in both cases.

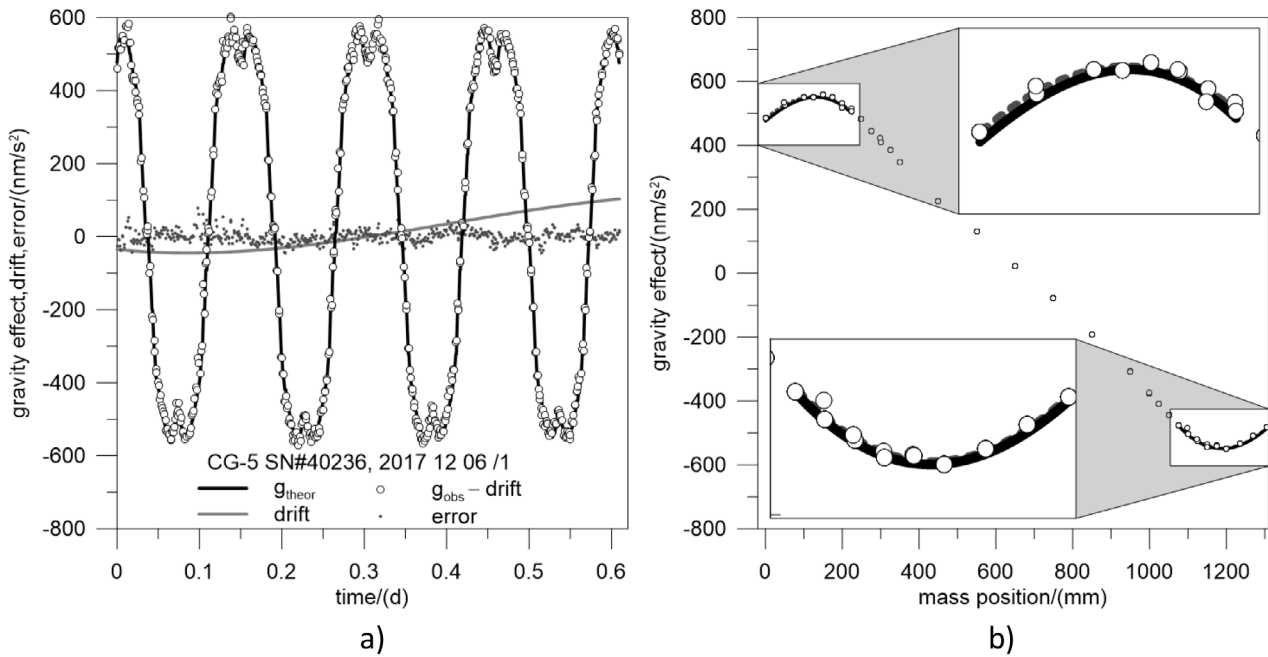


Figure 16. Calibration experiment 20171206/1 (CG-5 SN#070340236) applying the *Max-Min* approach. (a) Drift free observations (white circles), drift approached by a 2nd degree polynomial (grey solid line), residuals of adjusted gravity (small grey dots), theoretical signal (black solid line). (b) Adjustment of the extremes, adjusted polynomials: theoretical (black), observed (dashed gray), observations (white circles).

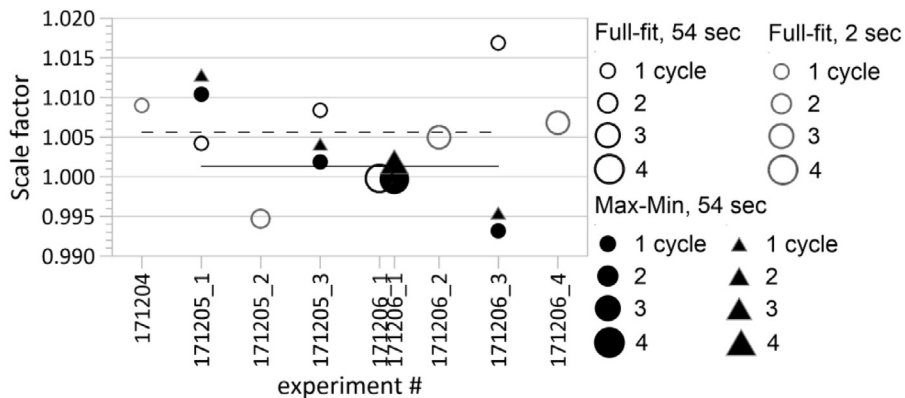


Figure 17. Results of the MMC for Scintrex CG-5. Grey dashed line: average over all Full-fit experiments, black solid line: average over all Max-Min experiments (filled circles). See text for explanation of filled circles/triangles .

7. Conclusions

The MMC device is able to generate fine and well controlled variations in the gravity field in a significantly narrower (typical tidal) range compared to the usual gravimeter calibration lines having a variation range of several 100 or 1000 $\mu\text{m s}^{-2}$. The overall accuracy of the reference signal provided by the facility operated in the Mátyáshegy Gravity and Geodynamic Observatory Budapest is certainly better than 5 nm s^{-2} which is sufficient for many kinds of instrument tests. Consequently the applied method gives an accurate solution for the calibration of both LCR and Scintrex CG-5 gravimeters used in tidal research and for the investigation of the sensor characteristics

of the instruments equipped with different reading utilities either or not supported by feed-back system.

The main advantage of the MMC against any other method is methodological. On one hand it provides the simplest metrological standard and on the other it satisfies the conditions of constrained centricity and synchrony derived from an extended interpretation (generalization) of Abbe principle of alignment. But these positive features can probably be exploited only for microgravimetry, where the range of the signals to be measured does not exceed significantly the range of the signal generated by the movement of the mass, for example in tidal research or in experiments relying on highly precise determination of spatial gravity differences like in

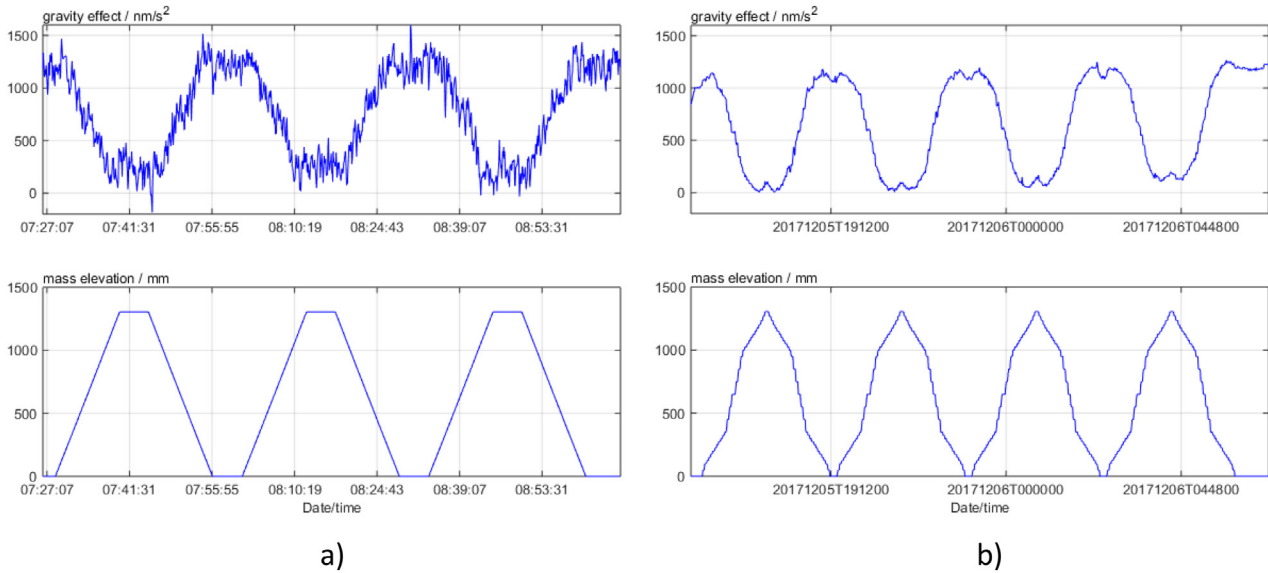


Figure 18. Calibration of Scintrex CG-5 (top: gravity g_z , bottom: mass position l_i). (a) with 5 s sampling rate (2 s integration interval and 3 s processing/data storage) and continuous mass movement. (b) with 1 min sampling rate (54 s integration interval and 6 s processing/data storage) and ‘stop-and-go’ mass movement. One full cycle consisted of 60 predefined steps with denser steps close to the gravitational extrema, i.e. in the range of 100–350 and 1000–1200 mm, therefore a full cycle lasted almost 4 h.

Table 7. The main error sources of the MMC method discussed in the paper and the estimated magnitudes of their effects.

Overall error of the calibrating signal due to the uncertainty of cylindrical ring parameters (figure 6, equation (15))		$\leq 3 \text{ nm s}^{-2}$
Instrumental/measuring errors	Error due to horizontal eccentricity of gravimeter sensor (figure 8(a))	$\leq 0.1 \text{ nm s}^{-2}$
	Non-random systematic effect of LCR G meters due to the rheology of the astaticized spring sensors (figure 15)	$\leq 20 \text{ nm s}^{-2}$
Correction errors	Accuracy of barometric correction (equation (17))	$\leq 1 \text{ nm s}^{-2}$
	Accuracy of the linear approximation used for joint tidal and drift correction (equation (18))	$\leq 3 \text{ nm s}^{-2}$
	Accuracy of magnetic effect (for metal spring gravimeters) (equation (19))	$\leq 2 \text{ nm s}^{-2}$
	Tilt correction of LCR instruments which are not equipped with feed-back system (equation (21))	$\leq 0.5 \text{ nm s}^{-2}$
Microseismic noise (supplementary material, figure 1)	LCR G meters (at 1 Hz sampling)	$\geq 10 \text{ nm s}^{-2}$
	Scintrex CG5 (at 0.5 Hz sampling)	$\geq 100 \text{ nm s}^{-2}$

watt balance experiments (Jiang *et al* 2013, Liard *et al* 2014). It cannot replace the traditional calibration lines although it may help the investigation of the instruments used to establish such lines below microgal level.

Both the calibration mode and the data processing method can be adjusted to the noise characteristics of the sensors and to the technology of data acquisition implemented in the gravity meters investigated. Continuous and stop-and-go-style movements of the test mass can be programmed and the observed data can be fitted using e.g. L2 norm to the theoretical signal at around the maximum and minimum places or along the whole observation set using the *Max-Min* or *Full-Fit* methods, respectively. Although theoretically the two solutions are equivalent slight systematic differences between the scale factors obtained by the application of the different processing methods were indicated in case of real LCR G observations (figure 14). When *Max-Min* is used the scale factors are always smaller than those provided by *Full-Fit* from the same observation set. It agrees with the results obtained from the analysis of simulated observations described in section 3.

The simulations draw attention to the unfavorable effect of environmental noise having even natural or technical origin showing a clear coupling between noise level and the *a posteriori* accuracy of calibration. But as section 6.1.2 indicated the residual signal provided by the *Full-Fit* method is not random exclusively since it correlates well with the second vertical derivative of the calibrating signal $\frac{\partial^2(\tilde{g})}{\partial t^2}$. Although it certainly biases all the estimated parameters s , g_0 and h_0 the bias of s is less than 1/1000 due to the robustness of this solution. The most probable reason of the systematic residuals is the response characteristic (rheology) of the spring type sensors, therefore it means a definite limit for the accuracy of calibration from the viewpoint of instrumental capabilities. The amplitude of this persistent and systematic residual signal is around 10 nm s^{-2} . It suggests that the relative calibration accuracy could not be better than 1% even if the accuracy of the calibrating signal was better by orders of magnitude. Despite—as it was demonstrated in the previous sections—the *a posteriori* accuracy of a scale factor of a single calibration experiment provided by *Full-Fit* method is rather (2–3) nm s^{-2} (0.2%–0.3%). It agrees

well with the error estimations given for the applied instrumental and environmental corrections. Although this accuracy is superior for spring sensors it could be increased further (at least to 1 nm s⁻²) because the effect of the systematic part of the residual signal can be eliminated in the calculations. This possibility, however, could only be exploited if a new MMC device was constructed based on the careful analysis of the accuracy estimates provided by this paper. The authors have already considered the possible improvements and made a proposal to build a new device capable to host the leading edge mobile instruments like GWR iGrav (R. Warburton personal communication) and Muquans Absolute Quantum (B. Desruelle personal communication) gravimeters and test their temporal stability at level below 1 nm s⁻² providing a uniform reference for the monitoring of *g* variations in the range of gravity tides. It is also worth to note that the pre-calculated cost of a dedicated laboratory and the moving mass apparatus proposed is less than that of a leading edge absolute or superconducting gravity meter. For easy referencing the main error sources forming the error budget of the calibration process is listed in table 7.

Acknowledgments

The authors are grateful for the financial support of NKFIH-OTKA K101603 project. Considering the maintenance operations and the latest upgrade of the MMC device the great help of László Merényi and Péter Kovács, Mining and Geological Survey of Hungary (former Eötvös Loránd Geophysical Institute) is appreciated. Special thanks to Krisztián Baracza (University of Miskolc, Faculty of Earth Science and Engineering) who was brave enough to test the feasibility of the MMC device with the Scintrex CG5 owned by Univ. Miskolc probably first in the world. The excellent technical support of Frigyes Bánfi and Tibor Molnár (Geodetic and Geophysical Institute, MTA CSFK, Sopron) during the calibration campaigns is also thanked. The professional encouragement of Richard Warburton (GWR Instruments Inc. USA) and Bruno Desruelle (Muquans, France) is acknowledged too. We gratefully acknowledge the helpful criticism and recommendations of two anonymous reviewers which helped to improve the paper.

Appendix

The partial derivatives of equation (14).

$$\begin{aligned} \frac{\partial(\bar{g})}{\partial h_0} = \tilde{g}'_{h_0} = 2G \frac{\Delta M}{L(r_2^2 - r_1^2)} & \left(\left((h_0 - l) \left((h_0 - l)^2 + r_1^2 \right)^{\frac{-1}{2}} \right) \right. \\ & - \left((h_0 - l + L) \left((h_0 - l + L)^2 + r_1^2 \right)^{\frac{-1}{2}} \right) \\ & - \left((h_0 - l) \left((h_0 - l)^2 + r_2^2 \right)^{\frac{-1}{2}} \right) \\ & \left. + \left((h_0 - l + L) \left((h_0 - l + L)^2 + r_2^2 \right)^{\frac{-1}{2}} \right) \right) \end{aligned} \quad (A.1)$$

$$\begin{aligned} \frac{\partial(\bar{g})}{\partial l} = \tilde{g}'_l = 2G \frac{\Delta M}{L(r_2^2 - r_1^2)} & \left(\left((l - h_0) \left((h_0 - l)^2 + r_1^2 \right)^{\frac{-1}{2}} \right) \right. \\ & - \left((l - h_0 - L) \left((h_0 - l + L)^2 + r_1^2 \right)^{\frac{-1}{2}} \right) \\ & - \left((l - h_0) \left((h_0 - l)^2 + r_2^2 \right)^{\frac{-1}{2}} \right) \\ & \left. + \left((l - h_0 - L) \left((h_0 - l + L)^2 + r_2^2 \right)^{\frac{-1}{2}} \right) \right) \end{aligned} \quad (A.2)$$

$$\begin{aligned} \frac{\partial(\bar{g})}{\partial L} = \tilde{g}'_L = 2G & \left(\frac{-\Delta M}{L^2(r_2^2 - r_1^2)} \left(\sqrt{(h_0 - l)^2 + r_1^2} \right. \right. \\ & - \sqrt{(h_0 - l + L)^2 + r_1^2} - \sqrt{(h_0 - l)^2 + r_2^2} + \sqrt{(h_0 - l + L)^2 + r_2^2} \left. \right) \\ & + \frac{\Delta M}{L(r_2^2 - r_1^2)} \left(- \left((h_0 - l + L) \left((h_0 - l + L)^2 + r_1^2 \right)^{\frac{-1}{2}} \right) \right. \\ & \left. + \left((h_0 - l + L) \left((h_0 - l + L)^2 + r_2^2 \right)^{\frac{-1}{2}} \right) \right) \end{aligned} \quad (A.3)$$

$$\begin{aligned} \frac{\partial(\bar{g})}{\partial r_1} = \tilde{g}'_{r_1} = 2G & \left(\frac{2\Delta M r_1}{L(r_2^2 - r_1^2)^2} \left(\sqrt{(h_0 - l)^2 + r_1^2} \right. \right. \\ & - \sqrt{(h_0 - l + L)^2 + r_1^2} - \sqrt{(h_0 - l)^2 + r_2^2} + \sqrt{(h_0 - l + L)^2 + r_2^2} \left. \right) \\ & \left. + \frac{\Delta M}{L(r_2^2 - r_1^2)} \left(r_1 \left((h_0 - l)^2 + r_1^2 \right)^{\frac{-1}{2}} - r_1 \left((h_0 - l + L)^2 + r_1^2 \right)^{\frac{-1}{2}} \right) \right) \end{aligned} \quad (A.4)$$

$$\begin{aligned} \frac{\partial(\bar{g})}{\partial r_2} = \tilde{g}'_{r_2} = 2G & \left(\frac{-2\Delta M r_2}{L(r_2^2 - r_1^2)^2} \left(\sqrt{(h_0 - l)^2 + r_1^2} \right. \right. \\ & - \sqrt{(h_0 - l + L)^2 + r_1^2} - \sqrt{(h_0 - l)^2 + r_2^2} + \sqrt{(h_0 - l + L)^2 + r_2^2} \left. \right) \\ & \left. + \frac{\Delta M}{L(r_2^2 - r_1^2)} \left(-r_2 \left((h_0 - l)^2 + r_2^2 \right)^{\frac{-1}{2}} + r_2 \left((h_0 - l + L)^2 + r_2^2 \right)^{\frac{-1}{2}} \right) \right) \end{aligned} \quad (A.5)$$

$$\begin{aligned} \frac{\partial(\bar{g})}{\partial(\Delta M)} = \tilde{g}'_{\Delta M} = -2G & \frac{1}{L(r_2^2 - r_1^2)} \left(\sqrt{(h_0 - l)^2 + r_1^2} \right. \\ & - \sqrt{(h_0 - l + L)^2 + r_1^2} - \sqrt{(h_0 - l)^2 + r_2^2} \\ & \left. + \sqrt{(h_0 - l + L)^2 + r_2^2} \right). \end{aligned} \quad (A.6)$$

ORCID iDs

G Papp  <https://orcid.org/0000-0001-6611-4578>

References

Achilli V, Baldi P and Casula G 1995 A calibration system for superconducting gravimeters *Bull. Géodésique* **69** 73–80
 Barta Gy, Hajósy A and Varga P 1986 Possibilities for the absolute calibration of recording gravimeters *Proc. of the Xth Int. Symp. on Earth Tides September 23–28, 1985 Madrid, Spain: with special sessions dedicated to ocean tides*, in Vieira R, Consejo superior de investigaciones científicas (CSIC), Madrid 27–34
 Benedek J 2016 Synthetic modelling of the gravitational field *Geomatikai Közlemények* **19** 7–105
 Benedek J, Kis M, Koppán A, Meurers B, Papp G, Szűcs E and Blaumoser N 2014 Comparative measurements of 3 relative spring gravimeters and the GWR SG025 for calibration purposes *COBS J.* **2014** 19
 Csapó G and Szatmári G 1995 Apparatus for moving mass calibration of LaCoste–Romberg feedback gravimeters *Metrologia* **32** 225–30

- Francis O, Niebauer T M, Sasagawa G, Klopping F and Gschwind J 1998 Calibration of a superconducting gravimeter by comparison with an absolute gravimeter FG5 in Boulder *Geophys. Res. Lett.* **25** 1075–8
- Götze H-J and Meurers B 1983 Some results of calibration factor determination of LaCoste and Romberg gravity meters (model D) *J. Geophys.* **52** 136–9
- Hinderer J, Florsch N, Makinen J, Legros H and Faller J E 1991 On the calibration of a superconducting gravimeter using absolute gravity measurements *Geophys. J. Int.* **106** 491–7
- Jiang Z et al 2013 On the gravimetric contribution to watt balance experiments *Metrologia* **50** 452–71
- Joglekar A-M 2003 *Statistical Methods for Six Sigma in R&D and Manufacturing* (New York: Wiley) p 344
- Liard J O, Sanchez C A, Wood B M, Inglis A D and Silliker R J 2014 Gravimetry for watt balance measurements *Metrologia* **51** 32–41
- Kanngieser E, Kummer K, Torge W and Wenzel H-G 1983 *Das Gravimeter–Eichsystem Hannover* Wissenschaftliche Arbeiten der Fachrichtung Vermessungswesen der Universität Hannover Nr. 120
- Meurers B 2012 Superconducting gravimeter calibration by collocated gravity observations: results from GWR C025 *Int. J. Geophys.* **2012** 12
- Meurers B 2018 Scintrex CG5 used for superconducting gravimeter calibration *Geod. Geodyn.* **9** 197–203
- Pálinkás V, Kašpar P and Lederer M 2003 Effect of the magnetic field on LCR gravimeters *Cahiers du ECGS* **22** 89–93
- Pálinkás V 2006 Precise tidal measurements by spring gravimeters at the station Pecný *J. Geodyn.* **41** 14–22
- Papp G, Szűcs E and Battha L 2012 Preliminary analysis of the connection between ocean dynamics and the noise of gravity tide observed at the Sopronbánfalva Geodynamical Observatory, Hungary *J. Geodyn.* **61** 47–56
- Papp G, Benedek J, Varga P, Kis M, Koppán A, Meurers B, Leonhardt R and Baracza M K 2018 Feasibility study applied to mapping tidal effects in the Pannonian basin—an effort to check location dependencies at μGal level *Geod. Geodyn.* **9** 237–45
- Riccardi U, Hinderer J, Boy J-P and Rogister Y 2009 Tilt effects on GWR superconducting gravimeters *J. Geodyn.* **48** 316–24
- Riccardi U, Rosat S and Hinderer J 2012 On the accuracy of the calibration of superconducting gravimeters using absolute and spring sensors: a critical comparison *Pure Appl. Geophys.* **169** 1343–56
- Richter B, Wilmes H and Nowak I 1995 The Frankfurt calibration system for relative gravimeters *Metrologia* **32** 217–23
- Setiawan A 2003 Modeling of gravity changes on Merapi volcano *PhD Dissertation D17* TU Darmstadt p 124
- Schnüll M, Röder R H and Wenzel H G 1984 An improved electronic feed-back system for LaCoste and Romberg gravity meters *B.G.I., Bull. d'Inf.* **55** 27–36
- Torge W 1989 *Gravimetry* (Berlin: de Gruyter)
- U.S. Standard Atmosphere 1976 U.S. Government Printing Office, Washington, D.C.
- Varga P, Hajósy A and Csapó G 1995 Laboratory calibration of Lacoste-Romberg type gravimeters by using a heavy cylindrical ring *Geophys. J. Int.* **120** 745–57
- Warburton R J, Beaumont C and Goodkind J M 1975 The effect of ocean tide loading on tides of the solid earth observed with the superconducting gravimeter *Geophys. J. R. Astron. Soc.* **43** 707–20
- Wenzel H G 1996 The nanogal software: earth tide data processing package eterna3.30 Bulletin d'Informations Marées Terrestres **124** 9425–39